

P-TEFb promotes cell survival upon p53 activation by suppressing intrinsic apoptosis pathway

Zhijia Wang¹, Monika Mačáková^{1,†}, Andrii Bugai^{1,2,†}, Sergey G. Kuznetsov³, Antti Hassinen⁴, Tina Lenasi¹, Swapnil Potdar³, Caroline C. Friedel⁵ and Matjaž Barborič^{1,*}

¹Department of Biochemistry and Developmental Biology, University of Helsinki, Helsinki FIN-00014, Finland,

²Department of Molecular Biology and Genetics, Aarhus University, 8000 Aarhus C, Denmark, ³High-Throughput Biomedicine Unit (HTB), Institute for Molecular Medicine Finland (FIMM), University of Helsinki, Helsinki FIN-00014, Finland, ⁴High Content Imaging and Analysis Unit (HCA), Institute for Molecular Medicine Finland (FIMM), University of Helsinki, Helsinki FIN-00014, Finland and ⁵Institute for Informatics, Ludwig-Maximilians-Universität München, 80333 Munich, Germany

Received November 23, 2022; Revised December 27, 2022; Editorial Decision December 30, 2022; Accepted January 03, 2023

ABSTRACT

Positive transcription elongation factor b (P-TEFb) is the crucial player in RNA polymerase II (Pol II) pause release that has emerged as a promising target in cancer. Because single-agent therapy may fail to deliver durable clinical response, targeting of P-TEFb shall benefit when deployed as a combination therapy. We screened a comprehensive oncology library and identified clinically relevant antimetabolites and Mouse double minute 2 homolog (MDM2) inhibitors as top compounds eliciting p53-dependent death of colorectal cancer cells in synergy with selective inhibitors of P-TEFb. While the targeting of P-TEFb augments apoptosis by antimetabolite 5-fluorouracil, it switches the fate of cancer cells by the non-genotoxic MDM2 inhibitor Nutlin-3a from cell-cycle arrest to apoptosis. Mechanistically, the fate switching is enabled by the induction of p53-dependent pro-apoptotic genes and repression of P-TEFb-dependent pro-survival genes of the PI3K-AKT signaling cascade, which stimulates caspase 9 and intrinsic apoptosis pathway in BAX/BAK-dependent manner. Finally, combination treatments trigger apoptosis of cancer cell spheroids. Together, co-targeting of P-TEFb and suppressors of intrinsic apoptosis could become a viable strategy to eliminate cancer cells.

INTRODUCTION

Gene transcription by RNA polymerase II (Pol II) is a highly regulated process that determines levels of gene expression and, by extension, nearly all facets of cellular identity, fate and metabolism. A central regulatory hub is the carboxy-terminal domain (CTD) of the largest subunit of Pol II, RPB1, which comprises heptad repeats with the consensus sequence Tyr¹Ser²Pro³Thr⁴Ser⁵Pro⁶Ser⁷ (1). During the transcription cycle, multiple positions within the CTD repeats are subject to dynamic phosphorylation and dephosphorylation events by transcriptional cyclin-dependent kinases (tCDKs) and phosphatases, respectively. These post-translational modifications modulate the binding of factors required for precursor mRNA (pre-mRNA) initiation, elongation, cotranscriptional maturation and termination, as well as chromatin modification (2,3).

Initiation of transcription is stimulated by CDK7, which is together with its regulatory partners cyclin H and Mat1 recruited to the Mediator-Pol II pre-initiation complex on gene promoters to phosphorylate Ser5 and Ser7 residues of the CTD. Concurrently, CDK7 promotes 5'-end capping of transcripts and facilitates promoter-proximal pausing of Pol II by stimulating the recruitment of DRB-sensitivity inducing factor (DSIF) and negative elongation factor (NELF), which bind and arrest Pol II in an inactive conformation (3,4). Critically, the release of paused Pol II into elongation genome-wide is triggered by the positive transcription elongation factor b (P-TEFb), composed of the catalytic CDK9 and a regulatory cyclin T1 or T2 subunit (5,6). P-TEFb phosphorylates Ser2 residues across the CTD and its linker, as well as multiple positions within both pause-inducing factors, converting DSIF into a positive elongation factor and triggering dissociation of NELF from

*To whom correspondence should be addressed. Tel: +358504482163; Email: matjaz.barboric@helsinki.fi

†The authors wish it to be known that, in their opinion, these authors should be regarded as Joint Second Authors.

Pol II. In turn, the polymerase associated factor complex (PAF_c) binds Pol II while SPT6 docks to the CTD linker region, allowing Pol II elongation to resume (7). Adding another layer of complexity, the P-TEFb-driven release of Pol II into elongation is opposed by phosphoprotein phosphatases, such as a protein phosphatase 2A (PP2A) complex, which is recruited to Pol II by the Integrator complex to dephosphorylate key P-TEFb substrates DSIF and the CTD of Pol II (8–11). Upon the release of Pol II from pausing, the homologous CDK12 and CDK13 interact with cyclin K to stimulate Pol II elongation throughout gene bodies and facilitate production of full-length transcripts through suppressing their premature cleavage and polyadenylation (12,13). Another set of well-studied tCDKs includes CDK8 and its CDK19 paralogue, which bind cyclin C to influence gene expression by phosphorylating transcription factors and controlling structure and function of the Mediator (14). Finally, CDK11 binds cyclins L1 and L2 to regulate transcription and pre-mRNA splicing by phosphorylating the CTD of Pol II and the U2 small nuclear ribonucleoprotein subunit SF3B1 (15,16).

Historically, transcription by Pol II has been deemed too essential to healthy cells for being considered as a target in cancer. Intriguingly, recent work shows that genetic and epigenetic alterations of cancer cells drive a transcriptionally deregulated state, referred to as transcriptional addiction, which facilitates tumor initiation and progression (17,18). In addition, hypertranscription, also called RNA amplification, is a newly appreciated hallmark of cancer that is frequently predictive of poor survival in multiple cancer types (19). Correspondingly, while absent in non-cancerous cells, these transcriptional alterations may instigate a disproportionate reliance on core components of the Pol II machinery to support tumor growth and survival, rendering cancer cells sensitive to perturbation of discrete phases of the transcription cycle (3,18). Indeed, recent work demonstrated that targeting CDK7, P-TEFb, and CDK12/13 with potent small-molecule inhibitors could lead to vigorous anti-tumor effects in xenograft and pre-clinical models of cancer (20–24). Importantly, while effective, the inhibitors of tCDKs imposed minimal toxicity to normal tissues. This is a considerable improvement over pre-clinical studies and/or clinical trials with pioneering pan-CDK inhibitors such as flavopiridol, which produced undesirable side effects including particularly concerning blood toxicities like neutropenia (25).

Despite hopeful prospects for targeting tCDKs in cancer, single-agent tCDK interventions may fail to culminate in durable responses due to therapeutic adaptation and/or presence of pre-existing tumor clones refractory to the therapy (26). Hence, tCDK-centered anti-cancer strategies could benefit when deployed as part of combination therapies. Because combining two compounds could target cancer cells in a synergistic manner, combination therapies enable compounds to be used at lower doses than as single agents, thus offsetting a potential for toxicity and resistance associated with a particular compound. Importantly, while single-agent therapies could lead to cytostatic response, combination approaches might trigger irreversible cell death, a desirable outcome of any effective cancer treatment (27,28).

In this study, we began addressing this issue by targeting P-TEFb which has emerged as a promising player in cancer (18,22,29). We screened a comprehensive library of oncology compounds to uncover those eliciting cell death in combination with a highly selective P-TEFb inhibitor NVP-2 that effectuates potent anti-cancer activity at non-toxic doses (30,31). This effort identified several clinically relevant groups of compounds, including top-performing antimetabolites and Mouse double minute 2 homolog (MDM2) inhibitors that activate tumor suppressor p53. By focusing on the pioneering MDM2 inhibitor Nutlin-3a, which dislodges the E3 ubiquitin ligase MDM2 from p53 (32) and thus promises to be a powerful anti-cancer agent for patients with wild-type (WT) p53 (33), we show that selective perturbation of P-TEFb converts the fate of Nutlin-3a-treated cells from cell-cycle arrest to apoptosis. Mechanistically, we uncover that the synthetic lethality of p53 activation and P-TEFb inhibition (PAPI) depends on activation of the intrinsic apoptosis pathway, which is enabled by induction of p53-dependent pro-apoptotic genes and repression of P-TEFb-dependent pro-survival genes encoding key components of the PI3K-AKT signaling cascade. Finally, we show that combination treatments of the PAPI framework remain effective in a three-dimensional cell culture setting, suggesting a translational potential of our work.

MATERIALS AND METHODS

Reagents

A list of reagents used in the study is provided in Supplementary Table S1.

Biological resources

HCT116 parental cell line and its derivatives were cultured in McCoy's 5A Medium (Sigma) and Dulbecco's Modified Eagle's Medium (Sigma) supplemented with 10% FBS and 100 U/ml penicillin/streptomycin. CCD 841 CoN cell line was cultured in Eagle's Minimum Essential Medium (Lonza) supplemented with 10% FBS and 100 U/ml penicillin/streptomycin. All cell lines were maintained at 37°C with 5% CO₂. Cell lines were confirmed regularly to be mycoplasma-free using a qPCR-based Mycoplasma check detection kit (Eurofins). Cell lines were not authenticated by us, but retrieved from trusted sources as listed in Supplementary Table S1D.

Chemicals

NVP-2, Nutlin-3a, 5-fluorouridine, 5-fluorodeoxyuridine, THZ531 and Pictilisib were from MedChemExpress. 5-fluorouracil, Senexin A, OTS964 and Triptolide were from Selleck Chemicals. YLK-5-124 and THAL-SNS-032 were a gift from Nathanael S. Gray's Laboratory (Stanford University, USA). iCDK9 was a gift from Qiang Zhou's Laboratory (University of California, Berkeley, USA). PP2A activator DT-061 was a gift from Jukka Westermarck's Laboratory (University of Turku, Finland).

FO5A oncology library screen and data analysis

FO5A version of the FIMM oncology collection was obtained from various commercial chemical vendors (34). The library comprised 527 single compounds and 1 drug combination, of which 28% represented approved anticancer drugs, 55%—emerging investigational compounds, and 17%—chemical probes covering a wide range of molecular targets (34) (Supplementary Figure S1A). Drug Sensitivity and Resistance Testing was performed as described previously (34) with minor modifications. Cytotoxicity was evaluated using CellTox Green Cytotoxicity Assay (Promega), whereby CellTox Green Dye was added to suspension of DMSO- and NVP-2-treated HCT116 cells that were seeded at 2000 cells/well on the 384-well plates containing the library's compounds in 25 μ l final volume using a BioTek MultiFlo FX microplate dispenser. After 72 h of incubation, fluorescence was measured with a Pherastar FS multi-mode plate reader (BMG Labtech) according to manufacturer's instructions. The cell viability data were processed using an in-house developed drug screening data analysis application Breeze (35). The data were normalized to negative control wells containing DMSO and positive control wells containing 100 μ mol/L benzethonium chloride that kills all cells. Drug sensitivity scores (DSS) (36) were calculated for each treatment. Differential DSS (dDSS) was further calculated by subtracting DSS values of NVP-2-containing plate sets from the values of DMSO-containing plate sets. Positive dDSS values indicated that NVP-2 enhances the cytotoxic effect of a given compound, while negative dDSS values suggest the opposite effect. The waterfall plots showing compounds having significant differences in dDSS across the screens were generated using R programming language with the help of package ggplot2.

Cytotoxicity, viability, apoptosis and caspase 9 activity assays

Cytotoxicity, viability, apoptosis and Caspase 9 activity assays were conducted using CellTox Green Cytotoxicity Assay (Promega), CellTiter-Glo 2.0 Cell Viability Assay (Promega), RealTime-Glo Annexin V Apoptosis and Necrosis Assay, and Caspase-Glo 9 Assay, respectively, according to manufacturer's instructions. For cytotoxicity, viability and apoptosis assays, HCT116 parental cell line and its derivatives were seeded at 20 000 cells/well on 96-well plates for 16 h and treated with the indicated compound combinations and corresponding volume of DMSO. For Caspase 9 activity assay, the parental and *BAX/BAK1*^{-/-} HCT116 cells were seeded at 8000 cells/well on 384-well plates for 6 h and treated with the indicated compound combinations. Fluorescence and luminescence measurements were taken at the indicated time points using PerkinElmer Victor X3 reader. Results from at least three independent experiments are presented as values relative to the values of DMSO-treated cells and plotted as the mean \pm s.e.m. For determining IC₅₀ value of NVP-2 in the presence and absence of Nutlin-3a and 5-FU, HCT116 cells were seeded at 5000 cells/well on 96-well plates for 6 h and treated with the indicated compounds for 72 h, after which cell viability was determined using CellTiter-Glo 2.0 Cell Viability Assay (Promega). Luminescence was measured using PerkinElmer

Victor X3 reader, and results from two independent experiments were normalized to the values of DMSO-treated cells and plotted as the average \pm s.d.

Data analysis of cytotoxicity and viability matrix assays

To obtain % of inhibition in cytotoxicity and viability assays, the raw fluorescence and luminescence values are presented as a ratio to the DMSO-treated control, normalized to the difference between DMSO and positive control sample representing maximum cytotoxicity. Maximum cytotoxicity was defined as a maximum fluorescence value obtained from the wells showing absolute cell death. An average of three independent experiments was plotted using the Seaborn Python data visualization library (<https://github.com/mwaskom/seaborn>). Bliss synergy scores were calculated using Synergyfinder (37).

Western blotting assay

Whole-cell extracts (WCE) were prepared using lysis buffer C (20 mM Tris-HCl, 0.5% NP-40, 150 mM NaCl, 1.5 mM MgCl₂, 10 mM KCl, 10% glycerol, 0.5 mM EDTA, pH 7.9) on ice for 1 h in the presence of EDTA-free Protease Inhibitor Cocktail (Sigma). Lysates were cleared by centrifugation at 20 000 g for 15 min, boiled in SDS running buffer supplied with 10% of β -mercaptoethanol for 5 min, separated using 10% SDS-PAGE and transferred to nitrocellulose membrane. For immunoblotting, the following antibodies were used according to manufacturers' instructions: anti-CDK9 (Santa Cruz Biotechnology, 1:4000); anti-p53 (Santa Cruz Biotechnology, 1:3000); anti-Cleaved PARP (Cell Signaling Technology, 1:3000); anti-p21 (Santa Cruz Biotechnology, 1:4000); anti-GAPDH (Santa Cruz Biotechnology, 1:10 000); anti-RNA polymerase II CTD repeat YSPTSPS (phospho S2) (Abcam, 1:3000); anti-RNA polymerase II RPB1 (Santa Cruz Biotechnology, 1:1000); anti-p110 α (Santa Cruz Biotechnology, 1:100); anti-p110 β (Santa Cruz Biotechnology, 1:500); anti-p85 α (Santa Cruz Biotechnology, 1:3000); anti-IRS-2 (Santa Cruz Biotechnology, 1:1000); anti-phospho-Akt (Ser473) (Cell Signaling Technology, 1:4000); anti-pan-Akt (Santa Cruz Biotechnology, 1:4000); anti-phospho-p44/42 MAPK (Erk1/2) (Thr202/Tyr204) (Cell Signaling Technology, 1:4000); anti-p44/42 MAPK (Erk1/2) (Cell Signaling Technology, 1:4000). Manufacturers provide validation for all antibodies.

RNA sequencing

Total RNA isolation and on-column digestion of genomic DNA was performed using the RNeasy Mini Kit (Qiagen) according to the manufacturer's instructions. RNA quality was assessed by TapeStation 4200 and samples with a RIN value of 10 were used for library preparation and sequencing. PolyA-selected libraries were made using NEBNext Poly(A) mRNA Magnetic Isolation Module and NEBNext Ultra Directional RNA Library Prep Kit (New England Biolabs) according to the manufacturer's instructions. The libraries were pooled and sequenced on one lane of an Illumina NextSeq500 (High Output 1 \times 75 bp; single-end).

Analysis of RNA sequencing datasets

RNA-seq reads were mapped against the human genome (hg38) and human rRNA sequences with ContextMap version 2.7.9 (38) using Burrows-Wheeler Alignment tool (39). Number of read counts per gene and exon were determined from the mapped RNA-seq reads in a strand-specific manner using featureCounts (40) and gene annotations from Gencode version 25 (41). Differential gene expression analysis was performed using edgeR (42). *P*-values were adjusted for multiple testing using the method by Benjamini and Hochberg (43) and genes with an adjusted *P*-value ≤ 0.001 were considered differentially expressed. For further analysis, we included only genes expressed (Reads per kilo base per million mapped reads (RPKM) ≥ 1) in at least condition. Analysis workflows were implemented and run using the Watchdog workflow management system (44). Volcano plots and heatmaps were created in R (<https://www.R-project.org/>). Hierarchical clustering analysis of genes in heatmaps was performed using Ward's clustering criterion (45) and Euclidian distances. Gene set enrichment analysis on log2 fold-changes for protein-coding genes was performed using the command line tool from <http://www.gsea-msigdb.org/> (version 4.0.2) (46) and hallmark gene sets from Molecular Signatures Database.

RNA extraction and RT-qPCR assay

HCT116 cells were seeded on 6-well plates for 16 h and treated at 80% confluency with the indicated compound combinations and corresponding volume of DMSO. RNA samples were extracted using TRI Reagent (Sigma), DNase-treated with the Turbo DNA-Free kit (Thermo Fisher Scientific), and reverse transcribed with M-MLV reverse transcriptase (Thermo Fisher Scientific) and random hexamers (Thermo Fisher Scientific) according to the manufacturers' instructions. qPCR reactions were performed with diluted cDNAs, primer pairs that spanned exon-exon junctions, and FastStart Universal SYBR Green QPCR Master (Rox) (Sigma) using Roche LightCycler 480. Primers were from Integrated DNA Technologies and designed using PrimerQuest Tool. Results from three independent experiments were normalized to the values of *GAPDH* mRNA and DMSO-treated cells, and plotted as the mean \pm s.e.m. Sequences of the primers used are listed in Supplementary Table S2.

Quantitative chromatin immunoprecipitation assay

ChIP-qPCR assay was performed as described previously (47) with the following modifications. HCT116 cells cultured on 15 cm plates were treated at approximately 80% confluency with DMSO or 20 nM NVP-2 for 3 h. Sixteen million cells were cross-linked with formaldehyde and the cell pellets were lysed in 800 μ l of RIPA buffer (50 mM Tris pH 8.0, 150 mM NaCl, 5 mM EDTA pH 8.0, 0.5% sodium deoxycholate, 1% NP-40, 0.1% SDS) in the presence of EDTA-free Protease Inhibitor Cocktail (Sigma). Lysates were sonicated with 12 cycles of 14 s sonication with the Misonix XL-2000 Ultrasonic Liquid Processor using the P-1 Microprobe 3.2 mm tip, power setting 10, in 1.7 ml RNase/DNase-free microcentrifuge tubes (Sigma),

which were kept for 1 min on ice between the cycles. After centrifugation at 13 000 *g* for 15 min, 30 μ l of the cleared chromatin was stored at -80°C for determining DNA input. The rest of the sample was divided in four equal parts, which were supplemented with additional 800 μ l of RIPA buffer and incubated overnight at 4°C with 15 μ l of antibody-coupled protein G Dynabeads (Thermo Fisher Scientific). Before adding the cleared chromatin, the beads were pre-blocked with bovine serum albumin and salmon sperm DNA overnight at a final concentration of 0.2 $\mu\text{g}/\mu\text{l}$, pre-incubated in 500 μ l of RIPA buffer for 4 h with the antibody and collected by magnetic stand to remove the unbound antibody. We used 2 μg of anti-RNA polymerase II RPB1 NTD (Cell Signaling Technology), 1 μg of anti-RNA polymerase II CTD repeat YSPTSPS (phospho S2) (Abcam) and 1 μg of anti-RNA polymerase II CTD repeat YSPTSPS (phospho S5) (Abcam) antibodies. Additionally, 2 μg of normal rabbit IgG (Santa Cruz Biotechnology) antibodies were used to determine specificity of the signals. Validation for all antibodies is provided on the manufacturers' websites. ChIP samples were dissolved in 30 μ l of water and 0.4 μ l of the solution was used per one qPCR reaction. DNA input was dissolved in 100 μ l of water, diluted 50 times, and 1 μ l of the solution was used per one qPCR reaction. Samples were amplified using FastStart Universal SYBR Green QPCR Master (Rox) (Sigma), DNA-specific primer pair, and LightCycler 480 II (Roche) machine. Primers were from Integrated DNA Technologies and designed using PrimerQuest Tool. Values were normalized to their levels in DNA inputs and the values of DMSO-treated cells. Ser2-P and Ser5-P ChIP values were further normalized to the values of total Pol II. Results from two independent experiments are presented as the mean \pm s.e.m. Sequences of the primers used are listed in Supplementary Table S3.

Confocal imaging of HCT116 spheroids and image analysis

HCT116 cell were seeded on 384-well, ultra-low attachment, Corning U-bottom, black clear-bottom imaging plates (Corning) at density of 400 cells/well and spun down at 200 *g* for 10 min. After culturing the cells for 48 h, the spheroids were treated with the indicated compound combinations for 96 h. Spheroids were stained with a freshly prepared PBS solution of 1 μM Calcein AM, 6 μM of DRAQ7 and 1x Hoechst 33342 (Invitrogen) for 6 h, after which imaging was performed with Opera Phenix confocal spinning-disk high-content screening microscope (PerkinElmer). Screening was conducted with a 40 \times water immersion objective. Fields of view were automatically selected from a pre-scan image with a 10% overlap using 90 pre-determined Z focus planes with laser-based autofocus. The images were captured with two Andor Zyla sCMOS cameras (Andor Technology). 3D Image analysis was performed with Harmony v4.9 High-Content Imaging and Analysis Software (PerkinElmer). Cells were segmented according to the Hoechst 33342 nuclear staining with a cytoplasmic mask from combined channel images. Results were quantified as a dead:live ratio of integrated intensities from DRAQ7 and Calcein AM staining in segmented cells and normalized against the observed cell number as

determined by Hoechst 33342 staining. Results of the normalized dead:live ratio values from three independent experiments were further normalized to the values of DMSO-treated cells and plotted as the mean \pm s.e.m.

Spheroid apoptosis assay

HCT116 cells were seeded at density of 400 cells/well on Nunclon Sphera 96-well U-bottom ultra low attachment 3D cell culture plate and spun down at 200 *g* for 10 min. After culturing the cells for 48 h to allow for spheroid formation, the spheroids were treated with the indicated compounds over the subsequent 48 h period. Apoptosis assay was conducted using RealTime-Glo Annexin V Apoptosis and Necrosis Assay (Promega) according to manufacturer's instructions. Luminescence measurements were taken at the indicated time points using PerkinElmer Victor X3 reader. Results from three independent experiments are presented as values relative to the values of DMSO-treated cells at 2 h and plotted as the mean \pm s.e.m.

Quantification and statistical analysis

Differential gene expression analysis of RNA-seq data was performed using edgeR (42). *P*-values obtained from edgeR were corrected by multiple testing using the method by Benjamini and Hochberg (43) for adjusting the false discovery rate (FDR) and an adjusted *P*-value cutoff of 0.001 was applied. Data shown for all qPCR-based experiments and functional assays were collected from at least three biological replicates as indicated in individual figure legends and are presented as means \pm s.e.m. Statistical significance and *P*-value were determined by Student's *t* test performed between the indicated paired groups of biological replicates. Where the results were not statistically significant, *P*-value are not indicated.

RESULTS

An oncology library screen identifies MDM2 inhibitors and antimetabolites as top compound classes that are synthetic-lethal with selective P-TEFb inhibitor NVP-2

To identify potentially therapeutic compounds that elicit synthetic lethality in combination with highly selective inhibitor of P-TEFb, we conducted an oncology library screen using HCT116 cell line, a well-established model of colorectal cancer encoding the oncogenic KRAS^{G13D} and PIK3CA^{H1047R} proteins (Figure 1A). We employed FO5A oncology library consisting of 528 investigational and clinical anti-cancer compounds (Supplementary Figure S1A), and NVP-2, an aminopyrimidine-derived ATP-competitive inhibitor of P-TEFb. We chose NVP-2 over other antagonists of P-TEFb due to its proven antitumor effect in a pre-clinical setting (30) as well as its superb potency and selectivity. Namely, NVP-2 inhibits the catalytic activity of P-TEFb and Ser2 phosphorylation of the Pol II CTD with half-maximal inhibitory concentration [IC₅₀] values of 0.5 and 4 nM, respectively, and displays at least 1200-fold lower activity toward CDK1, 2, 4 and 7 (31). To determine the dose of NVP-2 used in the screen, we exposed HCT116 cells to increasing concentrations of NVP-2 and measured

cellular viability with luminescence-based assay in which the number of metabolically active cells is determined by quantifying the levels of ATP via luciferase reaction. This approach revealed the IC₅₀ value of NVP-2 in HCT116 was 5 nM (Supplementary Figure S1B). As we aimed to identify compounds eliciting synergistic cell killing in combination with NVP-2, we elected to use 3 nM of NVP-2, which corresponded to its IC₃₀ dose.

We dispensed HCT116 cells together with DMSO or NVP-2 into 384-well plates containing the FO5A library compounds at five 10-fold serial dilutions. Upon culturing the cells for 72 h, we measured cellular response to the library compounds using fluorescence-based cytotoxicity assay, in which compromised membrane integrity of dead cells is proportional to fluorescence signal generated by the binding of an otherwise cell impermeable cyanine dye to DNA. To quantify cytotoxicity elicited by the treatments, we generated dose-response curves at each compound concentration and used these to calculate drug sensitivity score (DSS), an area under the dose-response curve type metric as described previously (48). To identify compounds eliciting cell death in combination with NVP-2, we calculated differential DSS (dDSS) value for each compound by subtracting the DSS values of DMSO-treated cells from NVP-2-treated cells, and considered dDSS values above 5 as effective. This analysis yielded 52 compounds, of which top seven groups include antimetabolites (*n* = 7), Mouse double minute 2 homolog (MDM2) inhibitors (*n* = 4), poly(ADP-ribose) polymerase (PARP) inhibitors (*n* = 4), Inhibitor of apoptosis (IAP) inhibitors/second mitochondria-derived activator of caspase (SMAC) mimetics (*n* = 3), farnesyl transferase inhibitors (*n* = 2), Aurora kinase inhibitors (*n* = 2) and Bromodomain and Extra-Terminal Domain (BET) inhibitor/degrader (*n* = 2) (Figure 1B and Supplementary Figure S1C). These findings indicate that selective targeting of P-TEFb heightens sensitivity of cancer cells to established anti-cancer compounds.

Amongst tCDKs, selective targeting of P-TEFb shows the most synergistic lethality with MDM2 inhibitors and antimetabolites

A common denominator of the two leading compound groups of our screen is activation of p53. While the identified antimetabolites are used as chemotherapeutics for a variety of cancers, clinical trials with MDM2 inhibitors have had only a limited success (33). Nevertheless, the long-standing quest in delivering these inhibitors into the clinic continues, particularly in the context of MDM2 combination therapies. Hence, in this study we investigated how MDM2 inhibitors and antimetabolites elicit synthetic lethality with selective targeting of P-TEFb. As representative compounds, we employed a pioneering MDM2 inhibitor Nutlin-3a and an antimetabolite fluoropyrimidine 5-fluorouracil (5-FU) throughout our work. Whereas Nutlin-3a acts as a competitive protein-protein interaction (PPI) inhibitor of the p53-MDM2 interface by mimicking three hydrophobic amino acid residues of p53 required for MDM2 binding (32), metabolites of 5-FU interfere with cellular metabolism via incorporating into RNA and DNA and inhibiting the nucleotide biosynthesis enzyme thymidy-

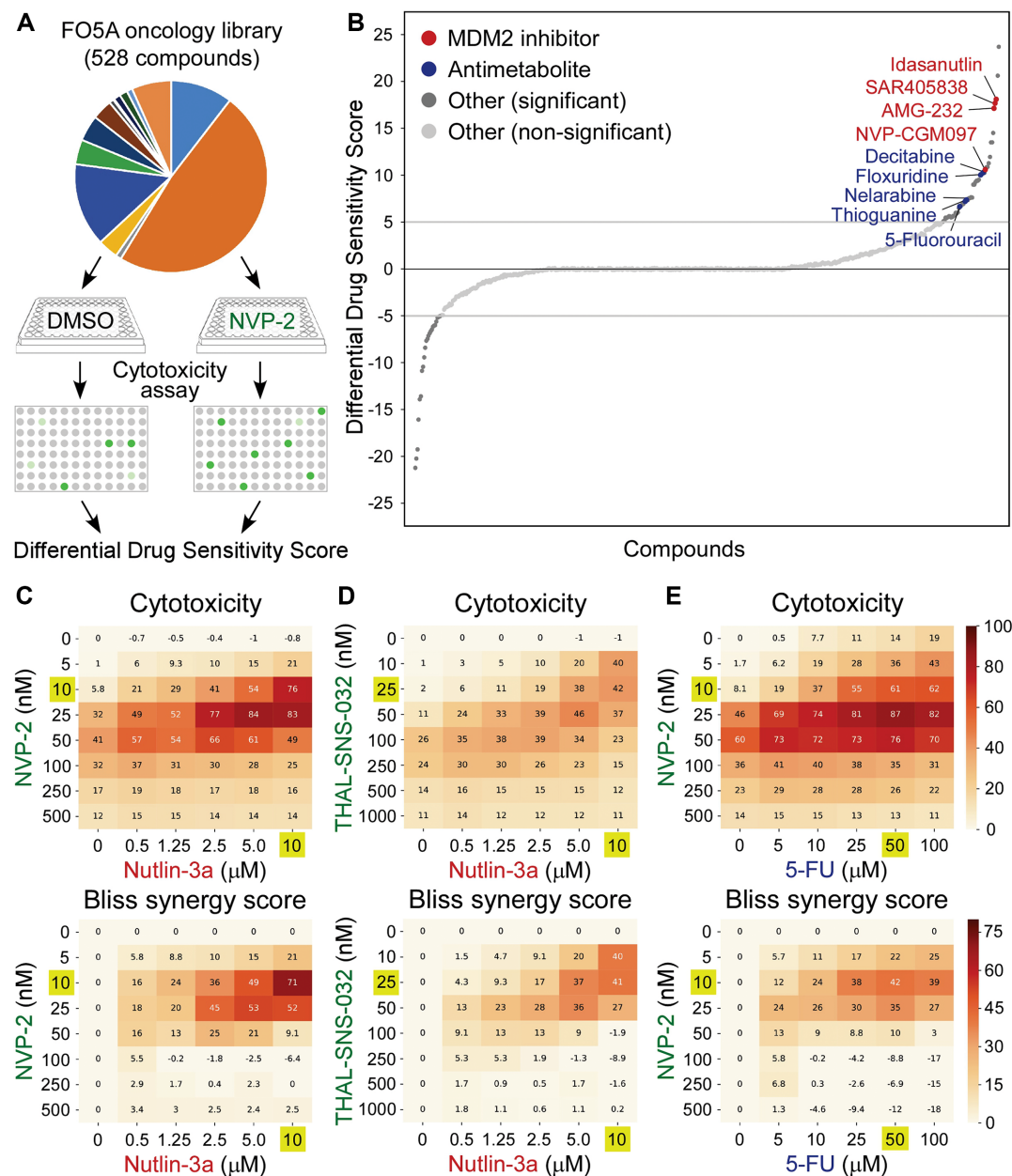


Figure 1. MDM2 inhibitors and antimetabolites are synthetic-lethal with selective perturbation of P-TEFb. (A) Workflow of the FO5A oncology library screen. DMSO- and NVP-2-treated HCT116 cells were exposed to the library compounds at five concentrations for 72 h, after which cytotoxicity was measured using CellTox Green assay and dDSS values were calculated. Dots indicate fluorescence readouts of specific FO5A library compound combinations. (B) Waterfall plot representing results of the screen. Compounds with dDSS values ≥ 5 and ≤ -5 were considered as significant. MDM2 inhibitors and antimetabolites are highlighted. (C–E) 8×6 cytotoxicity matrices with combinatorial titrations of NVP-2 and THAL-SNS-032 with Nutlin-3a and 5-fluorouracil (5-FU) at indicated doses to test for the synthetic lethality of compounds in HCT116 cells, depicting cytotoxicity (top) and synergy (bottom) of the combinations. Cytotoxicity values obtained at 48 h of the treatments using CellTox Green assay were normalized to the DMSO control and are presented as percentages of the maximum cytotoxicity which was set at 100%. Results represent the average of independent experiments ($n = 3$). Combinations with the highest Bliss synergy scores are highlighted.

late synthase (49). Even though both compounds activate the p53 pathway in HCT116 cells, non-genotoxic Nutlin-3a triggers reversible cell-cycle arrest in p53-dependent fashion (50), while genotoxic 5-FU elicits rapid p53-dependent apoptosis (51).

To confirm the screen results that MDM2 inhibitors and antimetabolites sensitize HCT116 cells to P-TEFb antagonists and to test for synergy of the combination treat-

ments, we first conducted cytotoxicity assays with combinatorial titrations of Nutlin-3a with NVP-2. Whereas Nutlin-3a alone did not show any cytotoxicity across the tested concentrations, it became highly toxic in the presence of sub-lethal doses of NVP-2 (Figure 1C). We next used Synergfinder (37) to determine Bliss synergy scores for all combinations. Here, Bliss score is a readout for synergy depicting the difference between expected effect, which assumes

the additive contribution of individual treatments, and observed effect, with positive scores indicating synergy of combination treatment. This analysis showed a striking degree of synergy between high doses of Nutlin-3a and low doses of NVP-2 in inducing lethality of HCT116 cells, wherein the combination treatment of 10 μ M of Nutlin-3a with 10 nM of NVP-2 was the most synergistic, reaching the Bliss score of 71 (Figure 1C, bottom). In contrast, despite induction of p53 by Nutlin-3a and decrease in the CTD Ser2 phosphorylation by NVP-2, combinations of Nutlin-3a with NVP-2 were not toxic to a non-transformed colorectal epithelial cell line CCD 841 CoN (Supplementary Figure S1D).

Because NVP-2 can engage CDK10 in addition to P-TEFb at 1 μ M dose (31), we next performed the same cytotoxicity and Bliss synergy score assays, but instead of NVP-2, we employed a selective CDK9 degrader THAL-SNS-032 or a highly selective ATP-competitive P-TEFb inhibitor iCDK9 to perturb the kinase (31,52). Confirming the results obtained with NVP-2, high doses of Nutlin-3a elicited synthetic lethality with low doses of THAL-SNS-032 and iCDK9 in a synergistic manner, reaching the highest Bliss scores of 41 and 38, respectively (Figure 1D and Supplementary Figure S1E). Likewise, increasing doses of 5-FU augmented sensitivity of HCT116 cells to sub-lethal doses of NVP-2, wherein the combination treatment of 50 μ M of 5-FU with 10 nM of NVP-2 resulted in the highest Bliss score of 42 (Figure 1E). Of note, cytotoxic effect of selective P-TEFb antagonists alone and in combination with p53 activators was biphasic (Figure 1C–E and Supplementary Figure S1E), suggesting that high doses of the antagonists lead to transcriptional shutdown that is incompatible with cell death. The biphasic response is reminiscent to the one effectuated by a pan-CDK inhibitor flavopiridol (53), which at high doses attenuates Pol II transcription globally (54,55).

To provide complementary evidence for the synthetic lethality triggered by PAPI, we conducted viability assays with combinatorial titrations of Nutlin-3a and 5-FU with NVP-2, and calculated Bliss synergy scores for all of the combinations. Corroborating the cytotoxicity results, both p53-activating compounds synergized with the sub-lethal doses of NVP-2 to decrease viability of HCT116 cells, reaching the Bliss scores of 49 and 42 with the combination treatments of 10 μ M of Nutlin-3a with 25 nM of NVP-2 and 50 μ M of 5-FU with 10 nM of NVP-2, respectively (Supplementary Figure S1F, G). Supporting these findings, 10 μ M of Nutlin-3a and 25 μ M of 5-FU decreased the IC₅₀ value of NVP-2 sharply, which dropped from 5 to 1.4 nM and 0.5 nM, respectively (Supplementary Figure S1B).

Finally, we asked whether specific pharmacological targeting of other major tCDKs can also induce synthetic lethality in combination with Nutlin-3a. We targeted CDK7, CDK8, CDK11 and CDK12/13 using YKL-5-124 (56), Senexin A (57), OTS964 (16,58) and THZ531 (59) inhibitors, respectively, and conducted the combinatorial cytotoxicity and Bliss synergy score assays. While targeting CDK8 was not cytotoxic to HCT116 cells, inhibitors of other tCDKs showed modest cytotoxicity in the absence of Nutlin-3a. Importantly, Nutlin-3a treatment elicited robust synthetic lethality only with the inhibitor of CDK7, reaching the highest Bliss score of 44 (Supplementary Fig-

ure S1H–K). This finding is consistent with a previous study which employed a chemical genetic approach as well as YKL-1-116, a precursor to YKL-5-124, to inhibit CDK7 in a selective manner (53). Interestingly, unlike P-TEFb antagonists, CDK7 inhibitors alone or together with Nutlin-3a and 5-FU continued to elicit cytotoxicity at higher doses (Supplementary Figure S1H) (53), which could reflect the reported lack of global downregulation of Pol II transcriptome upon CDK7 inhibition (53,56). Nevertheless, CDK7 inhibitors elicited highly synergistic cell death with p53 activators over a relatively narrow range (Supplementary Figure S1H) (53), which is similar to our results with P-TEFb antagonists. Together, these findings establish that p53 activating compounds Nutlin-3a and 5-FU elicit cytotoxicity of HCT116 cells in synergy with sub-lethal doses of highly selective antagonists of P-TEFb.

P53 is required for synthetic lethality of MDM2 inhibitor Nutlin-3a and antimetabolites with P-TEFb inhibitors

Because both Nutlin-3a and 5-FU impact cellular fate via p53, we next evaluated whether the observed synthetic lethality of PAPI depends on p53. To this end, we utilized the parental HCT116 cell line and its isogenic *TP53*^{−/−} derivative, in which *TP53* was inactivated by disrupting exon 2 of both alleles using recombinant adeno-associated virus (rAAV) vector methodology (60). We exposed these lines to combinatorial titrations of Nutlin-3a and 5-FU with NVP-2 and compared their cytotoxicity and viability profiles. While the lack of p53 lowered cellular sensitivity to increasing doses of all three compounds administered alone, it markedly blunted synthetic lethality of both p53 activators with NVP-2 (Figure 2A–D and Supplementary Figure S2A–D). Specifically, cytotoxicity of the highly synergistic combinations of Nutlin-3a and 5-FU with NVP-2 dropped in *TP53* null HCT116 cells by 5.7-fold and 7.1-fold, respectively, exemplifying the pivotal contribution of p53 to the synthetic-lethal phenotype (Figure 2E).

Because 5-FU exerts its anti-cancer effects in part through incorporation of its metabolites into RNA and DNA (49), we next asked whether its synthetic lethality with P-TEFb inhibition depends on RNA or DNA metabolism. To address this question, we utilized ribose and deoxyribose derivatives of 5-FU, 5-fluorouridine (5-FUR) or 5-fluorodeoxyuridine (5-FdUR), respectively. Of note, 5-FdUR, also called floxuridine, appeared among the top antimetabolites in our oncology library screen (Figure 1B and Supplementary Figure S1C) and is used to treat cancer of gastrointestinal tract that has metastasized to the liver. We therefore conducted cytotoxicity assays using the parental and *TP53* null HCT116 cells with combinatorial treatments of 5-FUR and 5-FdUR with NVP-2. We found that toxicity of both 5-FU derivatives was augmented in the presence of NVP-2 in p53-dependent fashion (Figure 2F), albeit its levels were lower in comparison to 5-FU (Figure 2E, F). These findings suggest that 5-FU exerts its synthetic lethality with P-TEFb antagonists through RNA and DNA metabolism. Together, p53 enables the synthetic lethality of Nutlin-3a and antimetabolites with P-TEFb antagonists, suggesting that cells become markedly dependent on P-TEFb upon activation of p53.

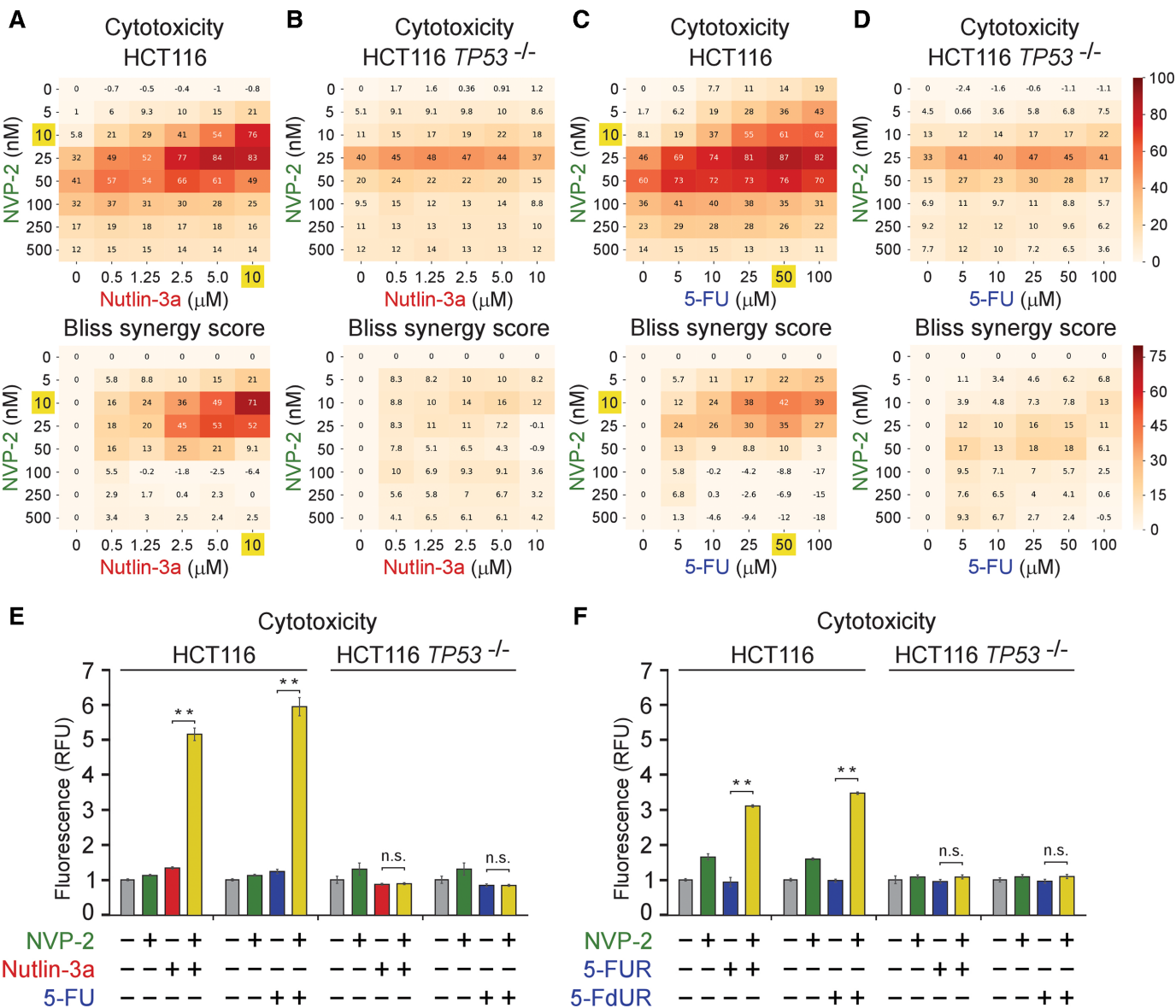


Figure 2. Synthetic lethality of Nutlin-3a and antimetabolites with P-TEFb inhibitor NVP-2 is p53-dependent. (A–D) 8 × 6 matrices with combinatorial titrations of NVP-2 with Nutlin-3a and 5-fluorouracil (5-FU) at indicated doses to test for the synthetic lethality of compounds in HCT116 and HCT116 *TP53*^{-/-} cells, depicting cytotoxicity (top) and synergy (bottom) of the combinations. Cytotoxicity values obtained at 48 h of the treatments using CellTox Green Cytotoxicity Assay were normalized to the values of DMSO-treated cells and are presented as percentages of the maximum cytotoxicity which was set at 100%. Results represent the average of independent experiments (*n* = 3). Combinations with the highest Bliss synergy scores in HCT116 cells are highlighted. (E,F) Cytotoxicity of HCT116 and HCT116 *TP53*^{-/-} cells treated with DMSO, NVP-2 (10 nM), Nutlin-3a (10 μM), and antimetabolites 5-Fluorouracil (5-FU, 50 μM), 5-fluorouridine (5-FUR, 0.5 μM) and 5-fluorodeoxyuridine (5-FdUR, 0.15 μM) alone and in combination as indicated for 48 h measured using CellTox Green Cytotoxicity Assay. Results are presented as fluorescence values relative to the values of DMSO-treated cells and plotted as the mean ± s.e.m. (*n* = 3). **, *P* < 0.01; n.s., non-significant, determined by Student's *t* test.

P53-dependent apoptosis drives synthetic lethality of p53 activation and P-TEFb inhibition

Upon activation, the DNA-binding transcription factor p53 elicits diverse anti-proliferative transcriptional programs, amongst which cell-cycle arrest and apoptosis are best understood (61). Based on the evidence gathered thus far, we hypothesized that following non-genotoxic and genotoxic stabilization of p53, perturbation of P-TEFb induces cell death by apoptosis. Therefore, when combined

with Nutlin-3a, targeting P-TEFb should convert cell fate choice from cell-cycle arrest to apoptosis, whereas augment apoptosis of cells exposed to sub-lethal doses of 5-FU. To address these predictions, we treated the parental and *TP53* null HCT116 cells with increasing doses of Nutlin-3a and 5-FU in the absence or presence of 10 nM of NVP-2. We next conducted immunoblotting analyses to monitor induction of apoptosis and p53 pathway by determining levels of caspase 3-cleaved poly(ADP-ribose) polymerase (cPARP)

and p53 along its direct transcriptional target, the CDK inhibitor p21, respectively. Indeed, while Nutlin-3a treatment of the parental HCT116 cells led to stabilization of p53 and induction of p21 in a dose-dependent manner, robust cleavage of PARP occurred exclusively in the presence of NVP-2 (Figure 3A, left). Similarly, the sub-lethal doses of 5-FU activated p53 but augmented cPARP levels only in combination with NVP-2 (Figure 3B, left). Importantly, none of these occurred in *TP53* null HCT116 cells (Figure 3A, B, right), once again underscoring the pivotal role of p53 in exerting synthetic lethality of PAPI. Confirming these findings, we observed the same apoptotic phenotype in HCT116 cells treated with Nutlin-3a and 5-FU in combination with selective P-TEFb antagonists THAL-SNS-032 and iCDK9 (Figure 3C, D and Supplementary Figure S3A).

To validate these immunoblotting findings and provide a kinetic view of apoptosis activation, we performed a luminescence-based quantitative assay that measures apoptosis-induced exposure of phosphatidylserine on the outer surface of cell membrane through time. The assay uses two Annexin V fusion proteins each containing a fragment of NanoBit Luciferase, of which complementation is achieved upon binding of Annexin V with phosphatidylserine (62). Compared to low levels of apoptosis elicited by Nutlin-3a and NVP-2 alone, we detected robust and p53-dependent apoptosis of cells exposed to the combination, starting to be apparent at about twelve hours of the treatment (Figure 3E).

Finally, we asked whether one functional *TP53* allele suffices to support activation of apoptotic cell death following concurrent p53 activation and P-TEFb inhibition. To this end, we performed the immunoblotting and kinetic apoptosis measurements by employing two additional isogenic HCT116 cell line derivatives constructed with the rAAV vector methodology. While the HCT116 *TP53*^{R248W/+} cell line contains WT and transcriptionally deficient *TP53* allele harboring R248W mutation found commonly in human cancers, the HCT116 *TP53*^{R248W/-} cell line lacks functional p53 (60). We treated both cell lines with increasing doses of Nutlin-3a in the absence or presence of 10 nM of NVP-2 and monitored the levels of cPARP, p53 and p21 by immunoblotting. As expected, Nutlin-3a treatment stabilized p53 in both cell lines, while p21 was induced only in HCT116 *TP53*^{R248W/+} cell line, underscoring the transcriptional competence encoded by the WT *TP53* allele (Supplementary Figure S3B). Critically, Nutlin-3a sensitized HCT116 *TP53*^{R248W/+} but not HCT116 *TP53*^{R248W/-} cells to NVP-2-induced apoptosis as documented by increased cleavage of PARP (Supplementary Figure S3B). Corroborating these findings, kinetic analyses showed robust activation of apoptosis by the combination of Nutlin-3a and NVP-2 over the single-agent treatments only in HCT116 *TP53*^{R248W/+} cells (Figure 3F). Of note, the magnitude of apoptosis induced by the combination treatment was approximately 2-fold lower compared to the one observed in parental HCT116 cells, whereas the kinetic profiles in both cell lines were very similar (Figure 3E, F). Together, p53-dependent apoptosis drives synthetic lethality of PAPI, whereby a single WT *TP53* allele is necessary for the effect.

P53-induced genes of the intrinsic apoptosis pathway remain expressed under sub-lethal inhibition of P-TEFb

Given the striking ability of P-TEFb antagonists to switch the fate of Nutlin-3a-treated HCT116 cells from undergoing cell-cycle arrest to apoptosis, we next set out to decipher a molecular basis for this phenotype. We reasoned that alterations in transcription could explain the exquisite dependency on P-TEFb following activation of p53. Therefore, we conducted RNA sequencing analysis (RNA-seq) of poly-A enriched pools of RNA isolated from HCT116 cells treated with DMSO, Nutlin-3a and NVP-2 in isolation, and in combination for eight hours, soon after which apoptosis is triggered by the combination treatment (Figure 3E). Based on the reproducible RNA-seq data (Supplementary Figure S4A), we determined differentially expressed genes ($P\text{-adj} \leq 0.001$; \log_2 fold-change ≥ 1).

We first analyzed transcriptional changes brought about by Nutlin-3a and examined how selective inhibition of P-TEFb by NVP-2 affected these changes. As expected, Nutlin-3a elicited a highly specific transcriptional program. In comparison to DMSO treatment, expression of only 1.08% of protein-coding genes was altered ($n = 10\,718$), amongst which 112 genes were induced, while four were repressed (Figure 4A). Using the hallmark gene set collection of the Molecular Signatures Database (46,63), gene set enrichment analysis revealed that the p53 Hallmark Pathway was the top upregulated gene set within the Nutlin-3a-regulated program (Supplementary Figure S4B), corroborating the selective targeting of the p53-MDM2 interface by Nutlin-3a. Importantly, the addition of NVP-2 to Nutlin-3a-treated cells significantly impacted expression of the Nutlin-3a-regulated genes (Figure 4B).

Because transcriptional activation by p53 is critical for triggering apoptosis (64), we next focused on the set of 112 genes induced by Nutlin-3a and quantified the impact of P-TEFb inhibition on these p53 targets. To this end, we calculated \log_2 fold-changes in expression for these genes in cells co-treated with Nutlin-3a and NVP-2 compared to Nutlin-3a treatment alone and created a heatmap with genes rank-ordered by decreasing changes in expression (Figure 4C). This analysis revealed that expression of 12 Nutlin-3a-induced genes increased further upon the addition of NVP-2, while expression of the remaining 100 genes either did not increase as much as with Nutlin-3a treatment alone (35 genes with \log_2 fold-change ≥ 1 compared to DMSO, 77 genes with \log_2 fold-change > 0) or decreased in expression compared to pre-Nutlin-3a levels (33 genes with \log_2 fold-change < 0 compared to DMSO). We next divided these 100 genes into four bins based on the magnitude of repression by NVP-2. Given that Nutlin-3a synergizes with NVP-2 to induce cell death by apoptosis, we reasoned that genes critical to the onset of apoptosis should not be exceedingly repressed by NVP-2. Indeed, we identified pro-apoptotic genes of the mitochondria-mediated intrinsic apoptosis pathway, including *AEN*, *BAX*, *BBC3* and *ATF3*, amongst genes showing no or little repression by NVP-2 (BIN 1), while another key member of this pathway, *APAF1*, was repressed only moderately (BIN 2).

BAX, *BBC3* and *APAF1*, which code for BCL-2-associated X protein (BAX), p53-upregulated modulator

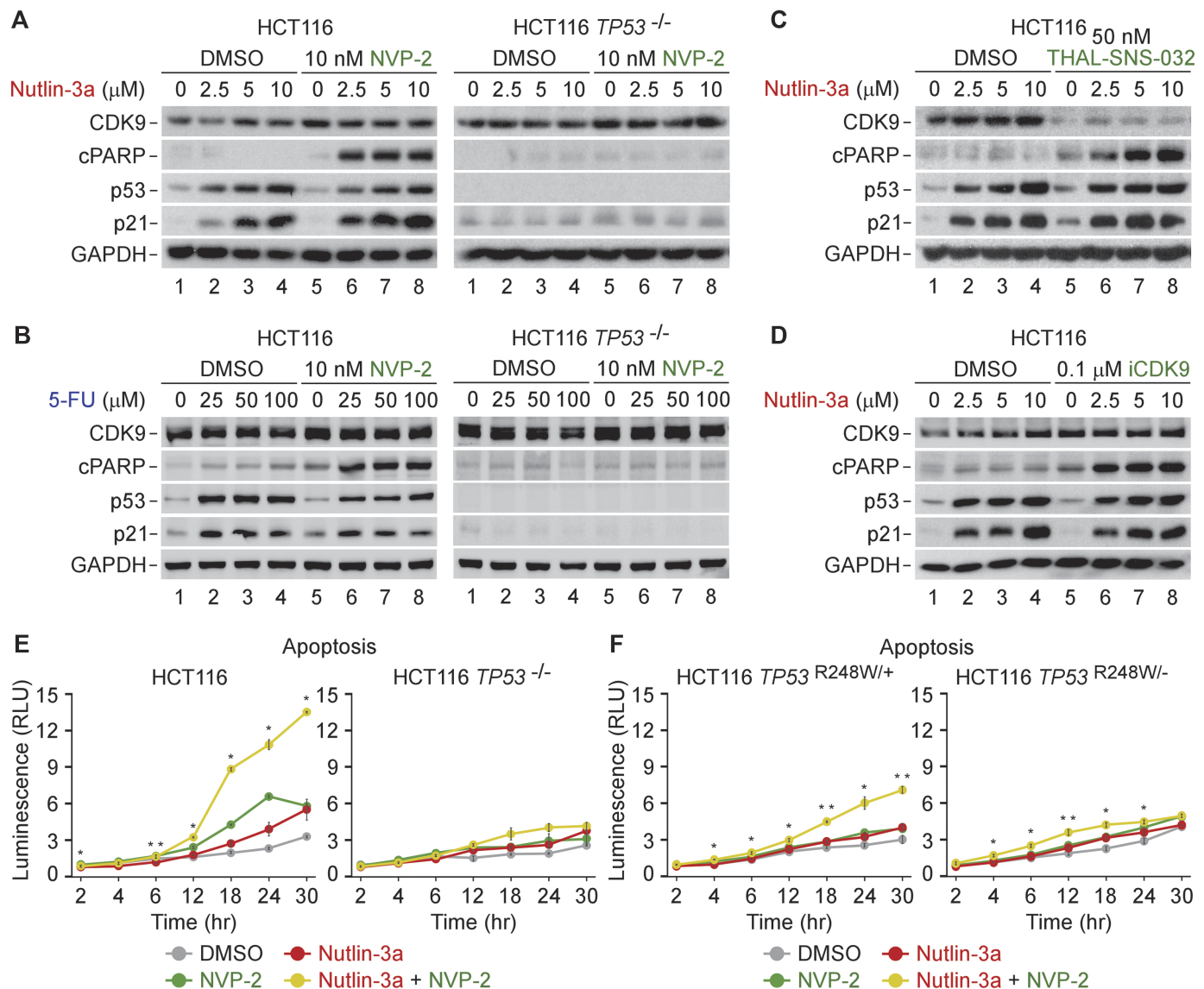


Figure 3. Activation of apoptosis underlies p53-dependent synthetic lethality of p53 activation and P-TEFb inhibition. (A–D) HCT116 and HCT116 *TP53*^{-/-} cells were treated with DMSO and indicated combinations and doses of P-TEFb antagonists, Nutlin-3a and 5-Fluorouracil (5-FU) for 24 h prior to preparation of whole cell extracts and detection of the indicated proteins by western blotting. (E,F) Apoptosis of the indicated HCT116 cell lines treated with DMSO, NVP-2 (10 nM) and Nutlin-3a (10 μM) alone and in combination. Results obtained at the time points indicated below the graphs using RealTime-Glo Annexin V Apoptosis and Necrosis Assay are presented as luminescence values relative to the values of DMSO-treated cells at 2 h and plotted as the mean ± s.e.m. (*n* = 3). *, *P* < 0.05; **, *P* < 0.01, determined by Student's *t* test using Nutlin-3a and Nutlin-3a + NVP-2 data sets.

of apoptosis (PUMA) and apoptotic protease-activating factor 1 (APAF1), respectively, are well-established regulators of the intrinsic apoptosis pathway (65). Here, the balance between pro-apoptotic and pro-survival members of the BCL-2 family of proteins governs mitochondrial outer membrane permeabilization (MOMP), the key commitment step to undergo apoptotic cell death (66). Specifically, pro-apoptotic members, such as BCL-2-interacting mediator of cell death (BIM), truncated BH3-interacting domain death agonist (tBID) and PUMA, can be bound and sequestered by pro-survival members such as BCL-2, B cell lymphoma extra large (BCL-X_L) or myeloid cell leukemia 1 (MCL1) (67). However, when these pro-survival proteins are saturated or absent, the balance is tipped in

favor of the pro-apoptotic members, enabling MOMP by the pore-forming BAX and BCL-2 antagonist/killer (BAK) oligomers, which releases apoptogenic molecules such as cytochrome *c* from the mitochondrial intermembrane space. In turn, cytochrome *c* binds APAF1 in the cytosol to assemble the heptameric apoptosome (68) that serves as a platform for autocleavage of the initiator procaspase 9, of which the active form leaves apoptosome to stimulate the downstream executioner caspases 3 and 7, culminating in dismantling of the cell.

Therefore, we next independently assessed our RNA-seq findings by conducting RT-qPCR analysis to determine mRNA levels of *BAX*, *BBC3* and *APAF1*. Because 10 μM of Nutlin-3a exhibited the highest synergy in elic-

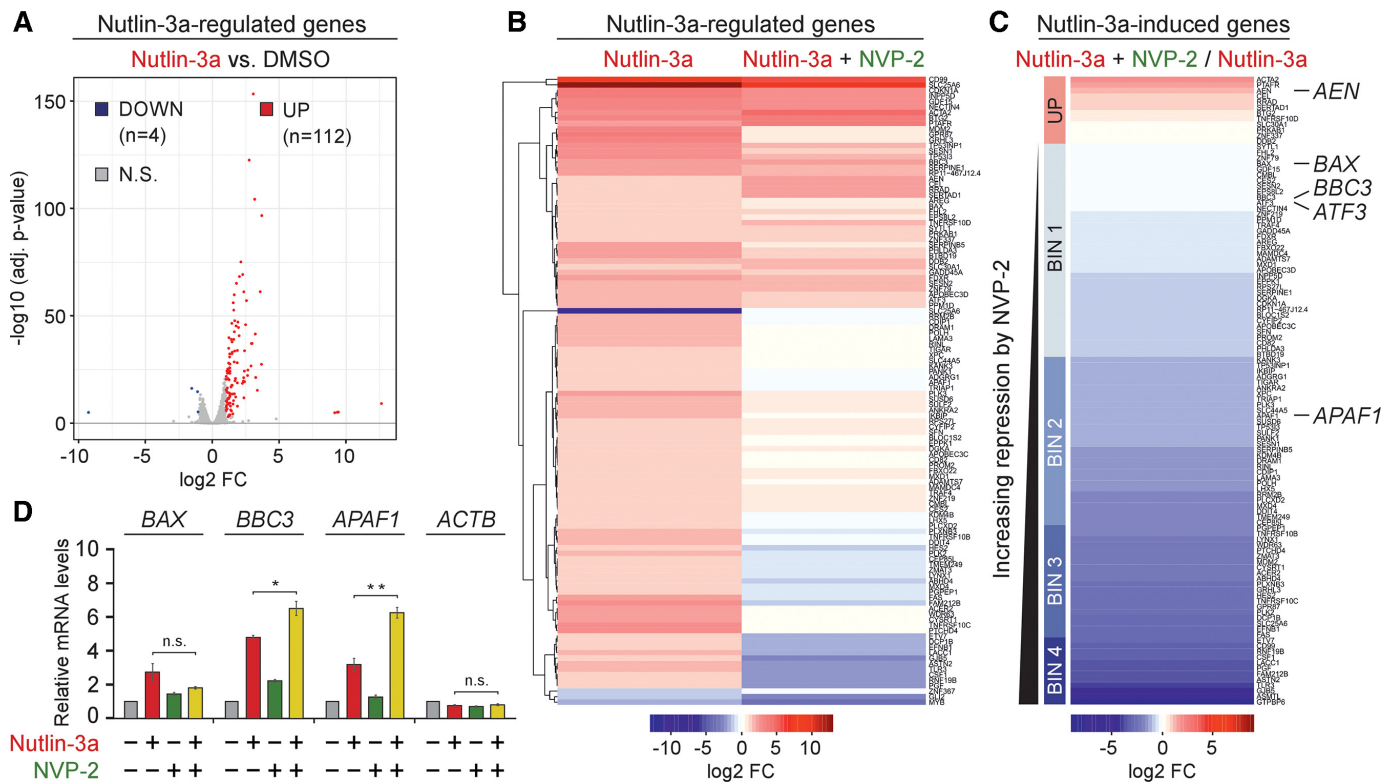


Figure 4. Sub-lethal inhibition of P-TEFb does not block p53-dependent induction of key pro-death genes of the intrinsic apoptosis pathway. (A) Volcano plot representation of differentially expressed protein-coding genes ($n = 116$, $P\text{-adj} \leq 0.001$, $\log_2 \text{FC} \geq 1$) from RNA-seq experiments ($n = 3$) of HCT116 cells treated with DMSO and 10 μM of Nutlin-3a for 8 h. Down-regulated (DOWN), up-regulated (UP) and non-significantly regulated (N.S.) genes are indicated. FC, fold-change. (B) Hierarchically clustered heatmap representation of Nutlin-3a-regulated protein-coding genes ($n = 116$, $P\text{-adj} \leq 0.001$, $\log_2 \text{FC} \geq 1$) from RNA-seq experiments ($n = 3$) of HCT116 cells treated with 10 μM of Nutlin-3a alone and in combination with 20 nM of NVP-2 for 8 h. Rows represent $\log_2 \text{FC}$ values of each gene under the depicted treatments on top relative to the values of DMSO-treated cells. FC, fold-change. (C) Heatmap representation of Nutlin-3a-induced protein-coding genes ($n = 112$, $P\text{-adj} \leq 0.001$, $\log_2 \text{FC} \geq 1$) from RNA-seq experiments ($n = 3$) in HCT116 cells treated with 10 μM of Nutlin-3a alone and in combination with 20 nM of NVP-2 for 8 h. Rows represent $\log_2 \text{FC}$ values of each gene under the Nutlin-3a + NVP-2 combination treatment relative to the values of Nutlin-3a-treated cells. Genes are sorted from largest to smallest $\log_2 \text{FC}$ values. UP labels genes induced by NVP-2 ($\log_2 \text{FC} > 0$). BIN 1 ($0 > \log_2 \text{FC} \geq -1$), BIN 2 ($-1 > \log_2 \text{FC} \geq -2$), BIN 3 ($-2 > \log_2 \text{FC} \geq -3$) and BIN 4 ($\log_2 \text{FC} < -3$) labels genes repressed by NVP-2. FC, fold-change. (D) HCT116 cells were treated with DMSO, Nutlin-3a (10 μM) and NVP-2 (10 nM) alone and in combination as indicated for 24 h prior to quantifying mRNA levels of the indicated genes with RT-qPCR. Results normalized to the levels of *GAPDH* mRNA and DMSO-treated cells are presented as the mean \pm s.e.m. ($n = 3$); *, $P < 0.05$; **, $P < 0.01$; n.s., non-significant, determined by Student's *t* test.

iting synthetic lethality with 10 nM of NVP-2 (Figure 1C), we exposed HCT116 cells to these treatments individually and in combination. As expected, treatment of the cells with Nutlin-3a induced these genes. Critically, the induced mRNA levels of *BAX* were decreased only moderately by NVP-2, while those of *BBC3* and *APAF1* were elevated further (Figure 4D). We noted that the sub-lethal dose of NVP-2 alone did not repress these genes but rather induced them slightly, suggesting that p53 opposes repression of key intrinsic apoptosis genes by NVP-2. To address this premise, we monitored their mRNA levels in the parental and *TP53* null HCT116 cells treated with increasing doses of NVP-2. In parental cells, the genes remained transcribed above basal levels or were induced even further by lethal doses of NVP-2 (Supplementary Figure S4C, left), which is consistent with a previous report that observed induction of a subset of p53-dependent genes, including *BAX* and *BBC3*, upon limited inhibition of P-TEFb (69). Strikingly, in the absence of p53, the genes get repressed potently and in a dose-dependent manner (Supplementary Figure S4C, right). Together, these findings show that sub-lethal

inhibition of P-TEFb does not hinder transcription of p53-induced genes that are instrumental for the intrinsic apoptosis pathway.

Intrinsic apoptosis pathway drives synthetic lethality of non-genotoxic p53 activation and P-TEFb inhibition in transcription-dependent manner

The above gene expression findings raised two inviting possibilities. First, the synthetic lethality of PAPI by Nutlin-3a and NVP-2 could be driven by activation of the intrinsic apoptosis pathway. Second, an efficient blockade of Pol II transcription should attenuate synthetic lethality of the combination treatment as induction of p53-dependent targets including key pro-apoptotic genes would not take place.

To address the requirement of the intrinsic apoptosis pathway for the synthetic lethality, we used the parental HCT116 cell line and its isogenic *BAX/BAK1*^{-/-} derivative that lacks the critical mediators of MOMP. We treated each cell line with 10 μM of Nutlin-3a and 10 nM of NVP-2

alone and in combination, and performed cytotoxicity assay. Strikingly, in contrast to the parental HCT116 cells, the *BAX/BAK1* null cells were completely resistant to cell death elicited by the combination treatment (Figure 5A). Furthermore, we monitored activity of the initiator caspase 9 in cell extracts of both cell lines exposed to the treatments by utilizing a luminescence-based quantitative assay that measures cleavage of a pro-luminogenic substrate by caspase 9. Critically, the combination treatment led to synergistic activation of caspase 9 in the parental cells, whereas the *BAX/BAK1* null HCT116 cells showed no activation (Figure 5B). Thus, the synthetic lethality of non-genotoxic p53 activation and P-TEFb inhibition depends on the intrinsic apoptosis pathway.

To determine whether the synthetic-lethal phenotype requires Pol II transcription, we first employed triptolide which inhibits Pol II transcription by blocking the ATPase activity of the TFIIH subunit XPB (70). Consistent with our prediction, triptolide blunted cell death of HCT116 cells exposed to the combinatorial titrations of Nutlin-3a with NVP-2 (Supplementary Figure S5A). To gather complementary evidence for this phenotype, we treated HCT116 cells with 10 μ M of Nutlin-3a and 10 nM of NVP-2 alone and together in the absence or presence of triptolide and monitored the levels of CDK9, cPARP, p53 and p21 by immunoblotting. While triptolide stabilized p53 across all conditions, it abrogated cleavage of PARP and induction of p21 (Figure 5C), confirming that blocking Pol II transcription is incompatible with apoptosis triggered by the combination treatment. Likewise, triptolide prevented activation of caspase 9 in cells co-treated with Nutlin-3a and NVP-2 (Supplementary Figure S5B). Importantly, we monitored mRNA levels of the intrinsic apoptosis genes *BAX*, *BBC3* and *APAF1* under the same treatments using RT-qPCR. Consistent with our cytotoxicity and apoptosis findings, triptolide ablated induction of *BAX*, *BBC3* and *APAF1* by the combination treatment (Figure 5D), the effect we recapitulated by substituting triptolide with the 500 nM dose of NVP-2 (Figure 5E). These findings are consistent with our initial observation that increasing the dose of P-TEFb antagonists beyond the one eliciting the maximal cytotoxicity precluded cell death when administered alone and in combination with Nutlin-3a or 5-FU (Figure 1 C–E and Supplementary Figure S1E–G). Corroborating this notion, the levels of cPARP and p21 peaked at 50 nM of NVP-2 and 500 nM of iCDK9, while higher doses of both inhibitors diminished these markers of apoptosis and p53-dependent transcription (Supplementary Figure S5C, D). Together, stimulation of the intrinsic apoptosis pathway drives the switch of Nutlin-3a-treated HCT116 cells from cell-cycle arrest to apoptosis, whereby p53-dependent induction of key pro-apoptotic genes plays a critical role.

Inhibition of P-TEFb hampers PI3K-AKT pathway via transcriptional repression of key components of PI3K signaling

While our findings thus far showed that the sub-lethal dose of NVP-2 did not impede a key element of the pro-apoptotic transcriptional program by p53, it remained unclear why do cells become markedly dependent on P-TEFb upon activation of p53. To this end, we next focused on transcriptional

changes elicited by NVP-2. Compared to Nutlin-3a, NVP-2 treatment had a much broader impact on gene expression, underscoring a pivotal role of P-TEFb in transcription by Pol II. Applying our criteria, we identified 22.69% differentially expressed protein-coding genes ($n = 10\,728$), amongst which 2137 genes were repressed, while 297 were induced (Figure 6A). These widespread alterations in transcription very likely affect many processes, some of which might promote switching the fate of Nutlin-3a-treated HCT116 cells. Nevertheless, we suspected that inhibition of P-TEFb might impact a key oncogenic pathway, stimulating apoptosis by the combination treatment.

Amongst the set of genes repressed by NVP-2, we were intrigued to find genes encoding key components of the oncogenic phosphoinositide 3-kinase (PI3K)–AKT signaling pathway, including class IA PI3K catalytic subunits p110 α (*PIK3CA*) and p110 β (*PIK3CB*), their regulatory subunit p85 α (*PIK3R1*), class II PI3K catalytic subunit C2 β (*PIK3C2B*), class III PI3K regulatory subunit p150 (*PIK3R4*) and a receptor tyrosine kinase (RTK) adaptor protein IRS-2 (*IRS2*) (Figure 6B). Namely, PI3K-AKT is the most commonly deregulated pathway in human cancers (71). Analyses across cancer lineages identified *PIK3CA* as the most frequently mutated single oncogene (72), of which the H1047R hotspot mutation within the kinase domain of p110 α , also present in HCT116 cells, circumvents the activation route of WT PI3K by promoting localization of the mutant kinase to plasma membrane (73). There, PI3K phosphorylates phosphatidylinositol 4,5-bisphosphate (PIP2) to produce the second messenger phosphatidylinositol 3,4,5-trisphosphate (PIP3), leading to the recruitment and full activation of the serine/threonine protein kinase AKT, promoting cell survival, growth and proliferation (Figure 6B). Importantly, AKT antagonizes intrinsic apoptosis pathway by phosphorylation of pro-apoptotic mediators BAD and caspase 9 (74).

We hypothesized that selective inhibition of P-TEFb interferes with the signaling through the PI3K-AKT pathway at the level of target gene transcription, thus contributing to apoptosis of Nutlin-3a-treated HCT116 cells. We first conducted RT-qPCR analysis using HCT116 cells treated with increasing doses of NVP-2 to assess mRNA levels of *PIK3CA*, *PIK3CB*, *PIK3R1*, *PIK3C2B*, *PIK3R4* and *IRS2*. In line with the RNA-seq results, we found that their levels decreased in a dose-dependent manner while those of *ACTB* remained unaffected (Figure 6C). In contrast, Nutlin-3a treatment had no impact on these genes (Supplementary Figure S6A), demonstrating that they are regulated independently of p53. As another control, we quantified mRNA levels of these genes in cells treated with increasing doses of the CDK7 inhibitor YKL-5-124 which were all toxic for the cells when administered alone or together with Nutlin-3a (Supplementary Figure S1H). With the exception of *IRS2*, their mRNA levels were largely unaffected by CDK7 inhibition (Supplementary Figure S6B), particularly when compared to the repression of the genes by NVP-2, suggesting that cellular sensitivity to CDK7 inhibitors upon p53 activation is not modulated through the PI3K-AKT pathway. To provide further evidence that P-TEFb promotes transcription of the PI3K-related genes, we next employed quantitative chromatin immunoprecip-

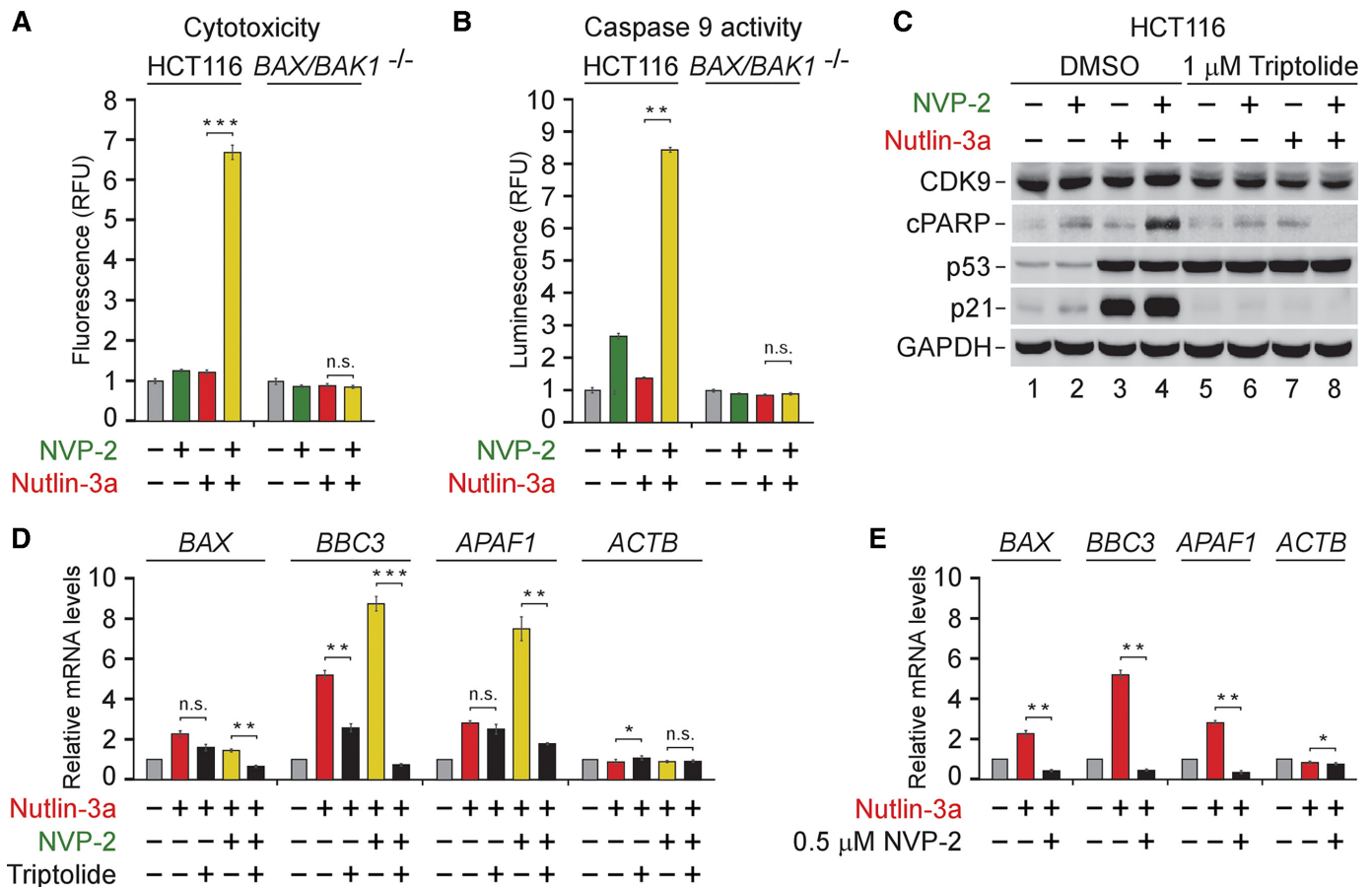


Figure 5. Synthetic lethality of non-genotoxic p53 activation and P-TEFb inhibition depends on intrinsic apoptosis pathway and on-going Pol II transcription. (A) Cytotoxicity of HCT116 and HCT116 *BAX/BAK1*^{-/-} cells treated with DMSO, NVP-2 (10 nM) and Nutlin-3a (10 μ M) alone and in combination as indicated for 48 h measured using CellTox Green Cytotoxicity Assay. Results are presented as fluorescence values relative to the values of DMSO-treated cells and plotted as the mean \pm s.e.m. ($n = 3$); ***, $P < 0.001$; n.s., non-significant, determined by Student's t test. (B) Activity of caspase 9 measured using Caspase-Glo 9 Assay in whole cell extracts of HCT116 and HCT116 *BAX/BAK1*^{-/-} cells treated with DMSO, NVP-2 (3 nM) and Nutlin-3a (10 μ M) alone and in combination as indicated for 18 h. Results are presented as luminescence values relative to the values of DMSO-treated cells and plotted as the mean \pm s.e.m. ($n = 4$). **, $P < 0.01$; n.s., non-significant, determined by Student's t test. (C) HCT116 cells treated with indicated combinations of NVP-2 (10 nM) and Nutlin-3a (10 μ M) were co-treated with DMSO and Triptolide as indicated for 24 h prior to preparation of whole cell extracts and detection of the indicated proteins by western blotting. (D) HCT116 cells were treated with DMSO, Nutlin-3a alone (10 μ M) and in combination with NVP-2 (10 nM) and Triptolide (1 μ M) as indicated for 24 h prior to quantifying mRNA levels of the indicated genes with RT-qPCR. Results normalized to the levels of *GAPDH* mRNA and DMSO-treated cells are presented as the mean \pm s.e.m. ($n = 3$); *, $P < 0.05$; **, $P < 0.01$; ***, $P < 0.001$; n.s., non-significant, determined by Student's t test. (E) HCT116 cells were treated with DMSO, Nutlin-3a (10 μ M) and NVP-2 (0.5 μ M) as indicated for 24 h prior to quantifying mRNA levels of the indicated genes with RT-qPCR. Results normalized to the levels of *GAPDH* mRNA and DMSO-treated cells are presented as the mean \pm s.e.m. ($n = 3$); *, $P < 0.05$; **, $P < 0.01$, determined by Student's t test.

itation (ChIP-qPCR) assays to monitor the occupancy of total Pol II as well as its CTD Ser2 and Ser5 phosphorylated forms at the transcription start site (TSS) and within gene body (GB) of three PI3K genes critical for the signaling through class IA PI3K using DMSO- and NVP-2-treated HCT116 cells. Namely, while CDK7 regulates Pol II transcription by phosphorylating Ser5 and Ser7 residues of the CTD (3), P-TEFb does so by targeting Ser2 residues (5,6). To account for the expected changes in Pol II occupancy at the genes elicited by NVP-2 (Supplementary Figure S6C), we normalized signals of the Ser2 and Ser5 phosphorylated forms to those of total Pol II. This analysis showed that treatment of the cells with a sub-lethal dose of NVP-2 resulted in significant drop of the CTD Ser2 but not Ser5 levels at most tested locations of *PIK3CA*, *PIK3R1* and *IRS2* (Figure 6D), confirming that NVP-2 decreases expression

of this set of PI3K-AKT pathway genes by targeting P-TEFb.

On the basis of these results, we reasoned that inhibition of P-TEFb should decrease protein levels of class IA PI3K heterodimers and adaptor protein IRS-2, leading to lowered activity of the PI3K-AKT signaling (Figure 6E). Because mTORC2 activates AKT by phosphorylating Ser473 (Ser473-P AKT) (71), we used phospho-specific antibody recognizing this AKT modification as a readout of PI3K-AKT pathway activation. Indeed, using immunoblotting analysis, we found that NVP-2 treatment decreased levels of p110 α , p110 β , p85 α and IRS-2 proteins in a dose-dependent fashion. Critically, these effects were accompanied by gradual attenuation of the PI3K signaling as determined by decreasing Ser473-P AKT levels, while total levels of AKT were affected minimally. In contrast, activ-

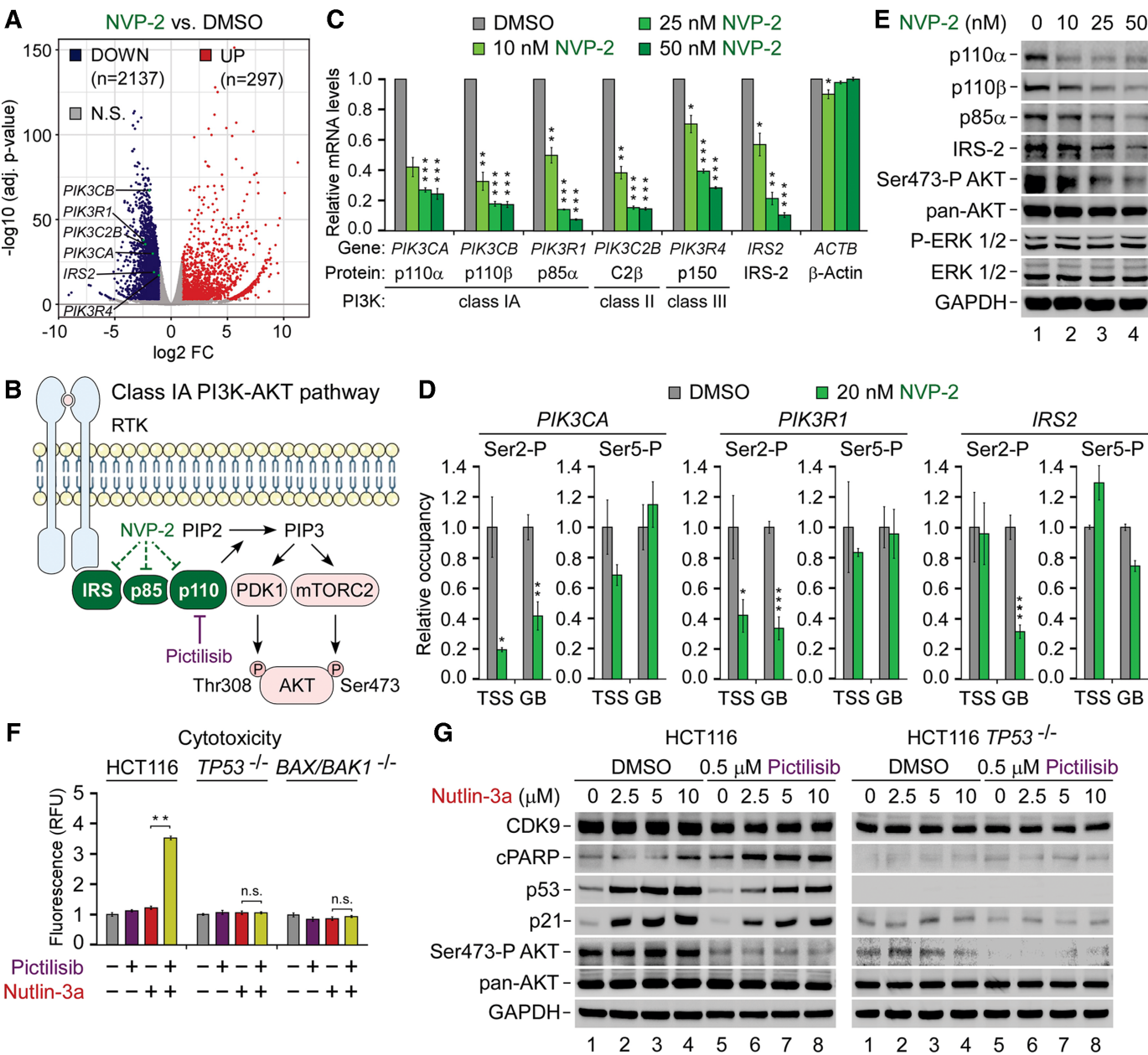


Figure 6. Repression of P-TEFb-dependent genes encoding key components of the pro-survival PI3K-AKT pathway is a driver of the synthetic lethality of p53 activation and P-TEFb inhibition. (A) Volcano plot representation of differentially expressed protein-coding genes (P -adj ≤ 0.001 ; \log_2 FC ≥ 1) from RNA-seq experiments ($n = 3$) of HCT116 cells treated with DMSO and 20 nM of NVP-2 for 8 h. Down-regulated (DOWN), up-regulated (UP) and non-significantly regulated (N.S.) genes are indicated. FC, fold-change. (B) Cartoon depicting Class IA PI3K-AKT pathway. Ligand-induced activation of transmembrane receptor tyrosine kinase (RTK) results in autophosphorylation on tyrosine residues, recruiting the PI3K catalytic subunit p110 α /p110 β /p110 δ to the membrane via PI3K regulatory subunits, such as p85 α , of which SH2 domains bind phosphotyrosyl residues on RTKs or adaptor proteins, e.g. IRS-2. Allosterically activated, PI3K phosphorylates phosphatidylinositol 4,5-bisphosphate (PIP2) to produce phosphatidylinositol 3,4,5-trisphosphate (PIP3). PIP3 acts as a second messenger to recruit the serine/threonine protein kinase AKT to the plasma membrane alongside phosphoinositide-dependent kinase-1 (PDK-1) and mechanistic target of rapamycin complex 2 (mTORC2), which activate AKT fully by phosphorylating Thr308 and Ser473, respectively. Dashed lines denote transcriptional repression of genes encoding IRS-2, p85 α and p110 by NVP-2. Pharmacological targeting of p110 α /p110 β /p110 δ by the pan-inhibitor of class I PI3K Pictilisib is indicated. (C) HCT116 cells were treated with DMSO and increasing doses of NVP-2 for 3 h prior to determining the levels of Ser2-P and Ser5-P forms relative to total Pol II at transcription start site (TSS) and gene body (GB) of the indicated genes with ChIP-qPCR. Results normalized to the values of DMSO-treated cells that were set to 1 are presented as the mean \pm s.e.m. ($n = 2$); *, $P < 0.05$, **, $P < 0.01$, ***, $P < 0.001$, determined by Student's t test. (D) HCT116 cells were treated with DMSO and NVP-2 (20 nM) for 3 h prior to determining the levels of Ser2-P and Ser5-P forms relative to total Pol II at transcription start site (TSS) and gene body (GB) of the indicated genes with ChIP-qPCR. Results normalized to the values of DMSO-treated cells that were set to 1 are presented as the mean \pm s.e.m. ($n = 2$); *, $P < 0.05$, **, $P < 0.01$, ***, $P < 0.001$, determined by Student's t test. (E) HCT116 cells were treated with DMSO and increasing doses of NVP-2 for 24 h prior to preparation of whole cell extracts and detection of the indicated proteins by western blotting. (F) Cytotoxicity of HCT116, HCT116 $TP53^{-/-}$ and HCT116 $BAX/BAK1^{-/-}$ cells treated with DMSO, Pictilisib (1 μ M), and Nutlin-3a (10 μ M) alone and in combination as indicated for 48 h measured using CellTox Green Cytotoxicity Assay. Results are presented as fluorescence values relative to the values of DMSO-treated cells and plotted as the mean \pm s.e.m. ($n = 3$); **, $P < 0.01$, n.s., non-significant, determined by Student's t test. (G) HCT116 and HCT116 $TP53^{-/-}$ cells were treated with DMSO and indicated combinations and doses of Pictilisib and Nutlin-3a for 24 h prior to preparation of whole cell extracts and detection of the indicated proteins by western blotting.

ity of the mitogen-activated protein kinase signaling pathway which we monitored using phospho-specific and total ERK1/2 antibodies did not change, highlighting specificity of P-TEFb requirement for the PI3K-AKT pathway. Together, we conclude that inhibition of P-TEFb hampers the oncogenic PI3K-AKT signaling cascade by repressing transcription of genes encoding key components of this pathway.

Pharmacological targeting of the PI3K-AKT pathway elicits synthetic lethality with activators of p53

The above findings suggested that decreased activity of the pro-survival PI3K-AKT pathway is a driver of heightened dependency on P-TEFb upon activation of p53. Hence, we hypothesized that direct pharmacological targeting of the PI3K-AKT pathway elicits synthetic lethality with non-genotoxic and genotoxic activators of p53. To address this prediction, we conducted cytotoxicity assays using the parental and *TP53* null HCT116 cells which we treated with Nutlin-3a, 5-FU, and a potent and selective inhibitor of class I PI3K Pictilisib (GDC-0941) alone or in combination (75). While all compounds provoked limited toxicity over the DMSO control when administered alone, Pictilisib treatment elicited synthetic lethality with both activators of p53 in a synergistic manner in parental but not *TP53* null cells, reaching the Bliss scores of 41 and 38 with Nutlin-3a and 5-FU, respectively (Figure 6F and Supplementary Figure S6D). Importantly, the lethality of non-genotoxic p53 activation and class I PI3K inhibition was abrogated in *BAX/BAK1* null HCT116 cells (Figure 6F), demonstrating the dependency on the intrinsic apoptosis pathway.

To extend these findings, we next tested whether attenuating PI3K-AKT pathway triggers p53-dependent apoptosis of HCT116 cells treated with Nutlin-3a. We exposed the parental and *TP53* null HCT116 cells to increasing doses of Nutlin-3a in the absence or presence of Pictilisib and performed immunoblotting analyses to monitor apoptosis as well as activity of p53 and PI3K-AKT pathways by determining levels of cPARP, p53, p21 as well as total and Ser473-P AKT. Indeed, while Nutlin-3a treatment of the parental HCT116 cells led to stabilization of p53 and induction of p21 in dose-dependent fashion in the absence or presence of Pictilisib, cPARP levels increased only upon blocking PI3K-AKT pathway (Figure 6G, left). We observed none of these in *TP53* null HCT116 cells (Figure 6G, right), highlighting the requirement of p53 for this synthetic lethality. Finally, co-treatment of HCT116 with Nutlin-3a and Pictilisib led to synergistic activation of caspase 9 in *BAX/BAK*-dependent manner (Supplementary Figure S6E). Together, these results demonstrate that inhibiting class I PI3K also switches the fate of Nutlin-3a-treated cells from cell-cycle arrest to apoptosis, whereby stimulation of the intrinsic apoptosis pathway plays a decisive role. As inhibition of ATM and MET kinases is synthetic-lethal with Nutlin-3a (76), our findings extend the list of signaling pathways that govern the choice of cell fate upon non-genotoxic activation of p53. Furthermore, these results confirm that compromising the PI3K-AKT pathway by transcriptional repression of its key components contributes to the synthetic lethality of PAPI.

Synthetic lethality of p53 activation and P-TEFb inhibition remains effectual in spheroid cultures

Three-dimensional spheroid cell cultures are a widely used platform for pre-clinical assessment of anti-cancer treatments (77). In contrast to monolayer cultures, spheroids possess several *in vivo* characteristics of tumor microenvironments, including well-organized spatial architecture of cells with different proliferation status, complex cell-cell contacts, oxygen and nutrient gradients, and rewired metabolism. Therefore, we assessed whether the synthetic-lethal combinations defined in this study remained effectual in HCT116 spheroids.

We established scaffold-free spheroids of about 400 μm in size and treated them for four days with DMSO, Nutlin-3a, 5-FU and NVP-2 alone and in combination as indicated (Figure 7A). To assess the viability of spheroids, we used confocal microscopy to image spheroids stained with a cocktail of three dyes. We identified live cells with an intracellular esterase activity indicator Calcein AM emitting green fluorescence, dead cells with a cell membrane impermeable DNA stain DRAQ7 emitting red fluorescence, and total cell nuclei with the cell membrane permeable DNA stain Hoechst emitting blue fluorescence. When administered alone, all compounds had a modest impact on spheroid viability and architecture. While both 5-FU and NVP-2 treatment resulted in limited toxicity, Nutlin-3a yielded spheroids with considerably less cells, indicative of p53-dependent cell-cycle arrest. Critically, both activators of p53 sensitized the spheroids to the sub-lethal dose of NVP-2 as evidenced by massive cell death that was accompanied by the loss of spheroid architecture (Figure 7A). To quantify viability of spheroids, we determined a ratio between dead and live cells for each spheroid by dividing intensities of Calcein AM and DRAQ7 staining in segmented cells, which we further normalized to the total spheroid cell number determined by Hoechst staining. Corroborating the confocal images, Nutlin-3a and 5-FU synergized with NVP-2 in eliciting death of spheroids (Figure 7B).

Finally, we conducted quantitative kinetic measurements to monitor apoptosis of spheroids exposed to combination treatments defined in this study as synthetic-lethal using monolayer cultures. We detected negligible levels of apoptosis when analyzing HCT116 spheroids treated for two days with Nutlin-3a, 5-FU, NVP-2 and Pictilisib. In contrast, the respective combination treatments elicited robust apoptosis in a highly synergistic manner (Figure 7C, E, G). As anticipated, p53 was required for this effect as the combinations failed to result in apoptosis of *TP53* null HCT116 spheroids (Figure 7D, F and Supplementary Figure S7A). Likewise, Nutlin-3a treatment sensitized HCT116 *TP53*^{R248W/+} but not p53-deficient HCT116 *TP53*^{R248W/-} spheroids to NVP-2 (Supplementary Figure S7B, C). In addition, both 5-FUR and 5-FdUR, the ribose and deoxyribose derivatives of 5-FU, elicited apoptosis in the presence of NVP-2 (Supplementary Figure S7D, E). Finally, within the canonical PAPI combination treatment, we replaced P-TEFb inhibitor NVP-2 with DT-061, a prototypical small-molecule activator of PP2A that stabilizes and allosterically activates a specific heterotrimeric PP2A holoenzyme which dephosphorylates key P-TEFb substrates including SPT5

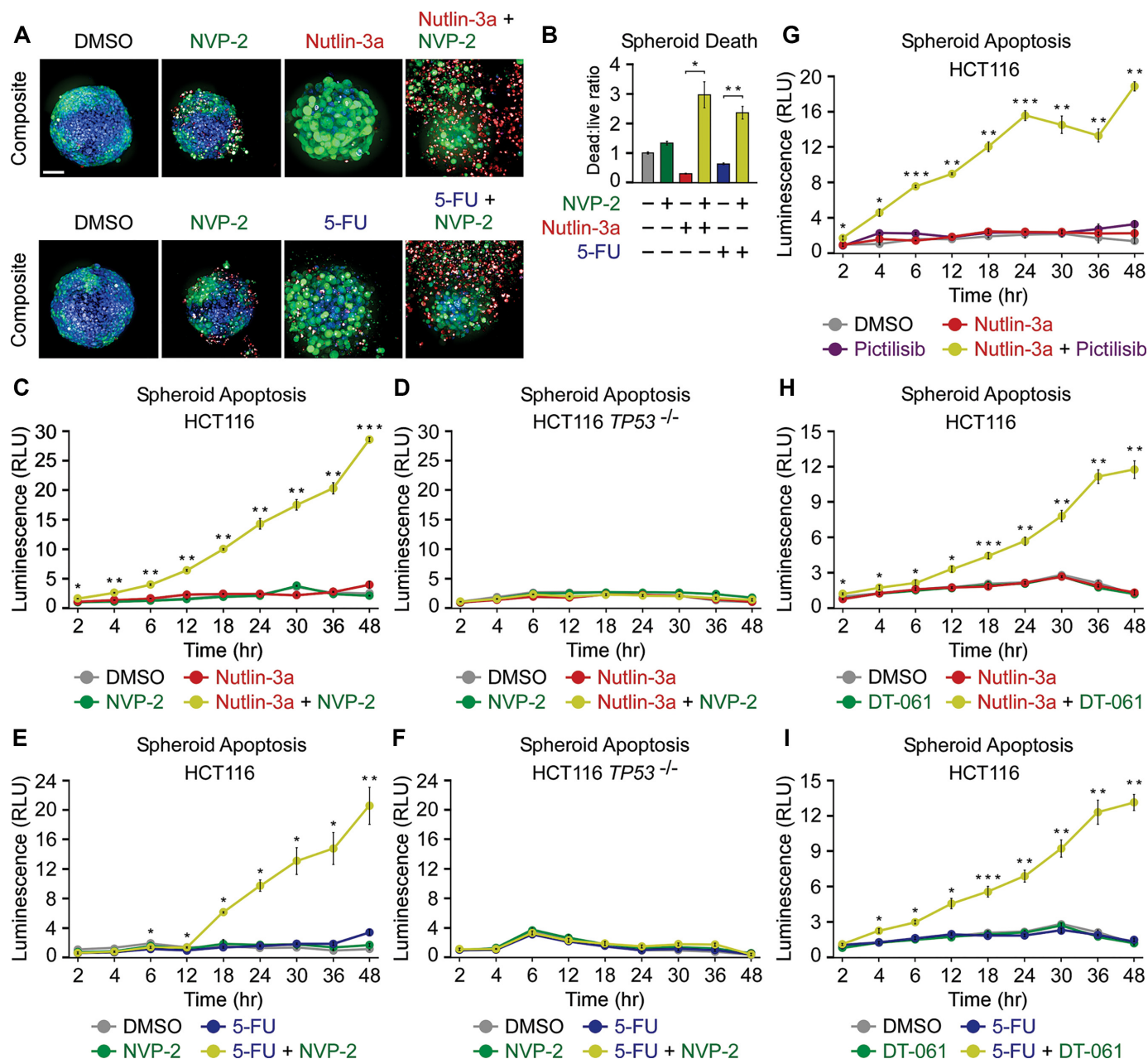


Figure 7. Combination treatments within the framework of p53 activation and P-TEFb inhibition trigger apoptosis of HCT116 spheroid cultures. (A) Representative composite images of HCT116 spheroid cultures treated with DMSO, NVP-2 (10 nM), Nutlin-3a (10 μ M) and 5-fluorouracil (5-FU, 25 μ M) alone and in the combinations as indicated. Spheroids were formed for 48 h, exposed to the treatments for 96 h and stained with Calcein AM (1 μ M), DRAQ7 (6 μ M) and Hoechst (1 \times) prior to confocal microscopy imaging; scale bar: 100 μ m. (B) Quantification of death of HCT116 spheroid cultures treated with DMSO, NVP-2 (10 nM), Nutlin-3a (10 μ M) and 5-fluorouracil (5-FU; 25 μ M) alone and in the combinations as indicated. Death of spheroids was determined as a ratio of integrated intensities from Calcein AM and DRAQ7 staining in segmented cells normalized to the total spheroid cell number quantified by Hoechst staining (dead:live ratio). The results presented as dead:live ratio values relative to the values of DMSO-treated cells are plotted as the mean \pm s.e.m. ($n = 3$); *, $P < 0.05$; **, $P < 0.01$, determined by Student's t test using Nutlin-3a and Nutlin-3a + NVP-2, and 5-FU and 5-FU + NVP-2 data sets. (C–I) Apoptosis of HCT116 and HCT116 *TP53*^{-/-} cell spheroid cultures treated with DMSO, NVP-2 (10 nM), Nutlin-3a (10 μ M), 5-Fluorouracil (5-FU, 25 μ M), Pictilisib (0.5 μ M) and DT-061 (10 μ M) alone and in combinations as indicated. Spheroids were formed for 48 h prior to the treatments. Results obtained at the time points indicated below the graphs using RealTime-Glo Annexin V Apoptosis and Necrosis Assay are presented as luminescence values relative to the values of DMSO-treated cells at 2 h and plotted as the mean \pm s.e.m. ($n = 3$). *, $P < 0.05$; **, $P < 0.01$; ***, $P < 0.001$, determined by Student's t test using Nutlin-3a and Nutlin-3a + NVP-2 (C, D), 5-FU and 5-FU + NVP-2 (E, F), Nutlin-3a and Nutlin-3a + Pictilisib (G), Nutlin-3a and Nutlin-3a + DT-061 (H), and 5-FU and 5-FU + DT-061 (I) data sets.

and the CTD of Pol II (10,78). We postulated that PP2A activation should akin to P-TEFb inhibition synergize with p53 activation in inducing apoptotic cell death. Indeed, non-genotoxic and genotoxic activation of p53 by Nutlin-3a and 5-FU, respectively, sensitized HCT116 spheroids to apoptosis by DT-061 (Figure 7H, I), illustrating possibilities to expand further the arsenal of synthetic-lethal combinations of PAPI. Together, we conclude that the synthetic-lethal combination treatments uncovered with monolayer cell cultures remained effectual in a translational spheroid setting.

DISCUSSION

The central role of tCDKs in gene control and their emergence as vital players in increasing number of cancer types has elevated the interest in these kinases as potential therapeutic targets. In this study, we harnessed a comprehensive oncology library to identify compounds that rendered colon cancer-derived cells dependent on Pol II transcription controlled by P-TEFb. Amongst the screen hits, we focused on antimetabolites and MDM2 inhibitors, the broadly used chemotherapeutics and small-molecule PPI inhibitors with a huge clinical potential, respectively, and uncovered a set of small-molecule combination treatments that triggered cell death by apoptosis in a synergistic and p53-dependent fashion. Importantly, we revealed that stimulation of the intrinsic apoptosis pathway drives cellular hypersensitivity to P-TEFb inhibition upon non-genotoxic stabilization of p53. Finally, we showed that combination treatments dismantled cancer cell spheroids by apoptosis, offering a rationale for further studies to assess effectiveness of the combinations in translational settings.

Our study contributes to the growing repertoire of synthetic-lethal interactions with inhibitors of P-TEFb. Previous work identified genetic and epigenetic alterations in cancer cells that heighten the reliance on P-TEFb. The prime examples are amplification of *MYC* and rearrangement of *MLL1*, whereby both oncoproteins redirect P-TEFb to their loci to drive oncogene-specific transcription programs, providing an explanation for increased sensitivity to P-TEFb inhibitors (18). In addition, perturbation of several targets, including BRD4 (52,79), PARP (80) and CDK2 (81) was reported to elicit lethality of cancer cells in combination with P-TEFb inhibitors. However, many of these studies employed inhibitors exhibiting sub-optimal selectivity towards P-TEFb, entailing a caveat that targeting of additional kinases contributed to the lethality. By conducting our screen with the highly selective inhibitor NVP-2, we here validated some of the previous reports and identified novel synthetic-lethal interactions. We revealed further that inhibiting class I PI3K and activating PP2A also sensitizes cancer cells to the representative p53-activating compounds Nutlin-3a and 5-FU. As PI3K and PP2A are important targets in cancer (71,82), our study offers new opportunities for the rational design of combination therapies that rely on functional p53.

Mechanistically, we uncovered a molecular basis that underpins the ability of P-TEFb inhibitor NVP-2 to switch the fate of Nutlin-3a-treated cells from cell-cycle arrest to apoptosis. Our evidence supports a model that differential sen-

sitivity of two key sets of genes to P-TEFb inhibition enables the fate switching. On the one hand, p53-dependent pro-death genes of the intrinsic apoptosis pathway remain expressed in the face of limited inhibition of P-TEFb. As complete P-TEFb blockade with higher doses of NVP-2 or attenuating Pol II transcription with triptolide diminishes cell death, continuous expression of these genes during sub-lethal inhibition of P-TEFb is critical for activating apoptosis. Our results indicate that p53 is a key factor that confers the resistance; in its absence, the genes become potently repressed. We speculate that the ability of p53 to override limited inhibition of P-TEFb stems from its powerful transactivation domains, which bind general transcription factors and a myriad of coactivators such as histone modifying enzymes, chromatin remodelers and Pol II elongation factors to stimulate multiple steps of target gene activation (83). On the other hand, however, pro-survival genes of the oncogenic PI3K-AKT signaling pathway that are not under the control of p53 get repressed, tipping the balance towards apoptotic cell death. Of note, PI3K-AKT pathway antagonizes apoptosis by phosphorylation and inhibition of pro-apoptotic mediators BAD and caspase 9, wherein AKT acts to release pro-survival BCL-2/BCL-X_L from BAD and to prevent cytochrome *c*-mediated activation of caspase 9, respectively (74). Therefore, we propose that following p53 activation, P-TEFb suppresses intrinsic apoptosis pathway in part by facilitating the signaling through the PI3K-AKT cascade at the level of the class IA PI3K gene transcription. Given the centrality of P-TEFb in transcription by Pol II (5), it is likely that its targeting impacts additional genes of which altered expression contributes to the activation of apoptosis.

By using a panel of selective inhibitors against major tCDKs, we found that besides P-TEFb, inhibition of CDK7 also elicited robust synthetic lethality in combination with Nutlin-3a. This observation confirmed an earlier report (53), which in addition uncovered that inhibiting CDK7 augmented apoptosis of HCT116 cells exposed to sub-lethal doses of 5-FU, thus providing another parallel to our experiments with targeting P-TEFb. Intriguingly, the synergy of CDK7 inhibition with both activators of p53 was driven by the death receptor-mediated extrinsic apoptosis pathway through Death Receptor 5 (DR5), a direct p53 target of which expression was refractory to CDK7 inhibition (53). Of note, high doses of 5-FU trigger the death of HCT116 cells by stimulating extrinsic apoptosis pathway via DR4 and DR5 (84,85). Although it remains to be determined how inhibition of P-TEFb augments apoptosis by sub-lethal doses of 5-FU, these findings nevertheless suggest that selective targeting of CDK7 and P-TEFb can sensitize cancer cells to p53 activators by stimulating both apoptosis-initiating pathways. In this context, co-targeting of CDK7 and P-TEFb could be beneficial in the tug-of-war, particularly because cancer cells evolve a multiplicity of strategies to short-circuit both modes of apoptosis activation (27,28). Supporting this premise, small molecules co-targeting casein kinase 1A1 (CKI α) as well as CDK7 and P-TEFb have a striking therapeutic effect in pre-clinical models of acute myeloid leukemia, whereby inhibition of CKI α activates p53 while co-inhibition of CDK7 and P-TEFb synergizes in stimulating apoptosis (20).

Our work provides grounds for improving antimetabolite-based chemotherapeutic interventions with the addition of highly selective antagonists of P-TEFb. Importantly, it promises to reinvigorate the ongoing efforts of reactivating tumor suppressive capabilities of p53 with Nutlin-3a-based combination therapies (33). Since the discovery of Nutlin-3a nearly 20 years ago, there has been a tremendous interest in delivering this class of non-genotoxic activators of p53 into the clinic. While up to a half of cancers carry *TP53* loss-of-function mutations in both alleles, the remaining half keep p53 in check through other means such as *MDM2* amplification, making WT p53 an appealing target for therapeutic intervention. However, Nutlin-3a and its derivatives elicit reversible cell-cycle arrest but not apoptosis in most cancer cell systems examined (50). Therefore, our findings on the fate switching of Nutlin-3a-treated cells by inhibitors of P-TEFb could come to the rescue. Because small-molecule MDM2 degraders are presumed to exhibit increased potency and therapeutic index over MDM2 inhibitors (86), combining the degraders with highly selective P-TEFb and PI3K antagonist or PP2A agonists warrants further investigation.

For over three decades, a goal of clinical oncology has been the development of therapies that promote elimination of cancer cells by apoptosis (27,28). Interestingly, our screen also identified SMAC mimetics amongst the top compounds that cooperate with NVP-2 in cancer cell killing. By mimicking the action of SMAC that gets released into the cytosol during MOMP, SMAC mimetics target pro-survival IAP proteins to facilitate cell death by promoting caspase 3, 7 and 9 activity (87). We therefore envision that targeting P-TEFb in combination with many suppressors of intrinsic apoptosis pathway could become a viable therapeutic strategy for irreversible demise of cancer cells.

DATA AVAILABILITY

All data associated with this study are presented in the main manuscript or the Supplementary Data. Materials that support the findings of this study are available from the corresponding author upon request. The RNA-seq data have been deposited to Gene Expression Omnibus (GEO) repository (NCBI) under the accession code GEO: GSE216610.

SUPPLEMENTARY DATA

Supplementary Data are available at NAR Online.

ACKNOWLEDGEMENTS

We thank Joaquin M. Espinosa for sharing parental and HCT116 *TP53*^{-/-} cell lines; Bert Vogelstein for sharing HCT116 *TP53*^{R248W/+} and HCT116 *TP53*^{R248W/+} cell lines; Ana J. Garcia-Saez for sharing HCT116 *BAX/BAK1*^{-/-} cell line; Qiang Zhou for sharing i-CDK9; Nathanael S. Gray for sharing YLK-5-124 and SNS032-THAL; Jukka Westermarck for sharing DT-061; FIMM High Throughput Biomedicine Unit for executing the FO5A screen and data analysis; FIMM High Content

Imaging and Analysis Unit for confocal imaging and analysis; Biomedicum Functional Genomics Unit at the University of Helsinki for RNA-seq.

Author contributions: M.B. and A.B. conceptualized the study and were assisted by Z.W. and M.M. in experimental design. M.B. supervised the study. S.G.K. designed and executed the FO5A screen with the assistance of M.B. S.P. analyzed the FO5A screen data and generated the associated waterfall plots. A.B. performed and analyzed all combinatorial titration cytotoxicity and viability assays and generated the associated heatmaps. M.M. conducted caspase 9 activity and cytotoxicity assays in the parental and HCT116 *BAX/BAK1*^{-/-} cell lines, and spheroid viability experiments. A.H. imaged the spheroids and analyzed the data. T.L. performed ChIP-qPCR assays. C.C.F. analyzed RNA-seq data and generated the associated volcano plots and heatmaps. All other experiments were performed and analyzed by Z.W. M.B. wrote the manuscript.

FUNDING

Sigrid Juselius Foundation [4707979 to M.B.]; Academy of Finland [1309846 to M.B.]; Cancer Foundation Finland [4708690 to M.B.]; Deutsche Forschungsgemeinschaft (DFG) [FR2938/9-1 and FR2938/10-1 to C.C.F.]. FIMM High-Throughput Biomedicine unit and FIMM High Content Imaging and Analysis unit were financially supported by HiLIFE, University of Helsinki, and Biocenter Finland. Funding for open access charge: Helsinki University Library.

Conflict of interest statement. None declared.

REFERENCES

- Eick,D. and Geyer,M. (2013) The RNA polymerase II carboxy-terminal domain (CTD) code. *Chem. Rev.*, **113**, 8456–8490.
- Bentley,D.L. (2014) Coupling mRNA processing with transcription in time and space. *Nat. Rev. Genet.*, **15**, 163–175.
- Parua,P.K. and Fisher,R.P. (2020) Dissecting the Pol II transcription cycle and derailing cancer with CDK inhibitors. *Nat. Chem. Biol.*, **16**, 716–724.
- Vos,S.M., Farnung,L., Urlaub,H. and Cramer,P. (2018) Structure of paused transcription complex pol II-DSIF-NELF. *Nature*, **560**, 601–606.
- Core,L. and Adelman,K. (2019) Promoter-proximal pausing of RNA polymerase II: a nexus of gene regulation. *Genes Dev.*, **33**, 960–982.
- Zhou,Q., Li,T. and Price,D.H. (2012) RNA polymerase II elongation control. *Annu. Rev. Biochem.*, **81**, 119–143.
- Vos,S.M., Farnung,L., Boehning,M., Wigge,C., Linden,A., Urlaub,H. and Cramer,P. (2018) Structure of activated transcription complex pol II-DSIF-PAF-SPT6. *Nature*, **560**, 607–612.
- Huang,K.L., Jee,D., Stein,C.B., Elrod,N.D., Henriques,T., Mascibroda,L.G., Baillat,D., Russell,W.K., Adelman,K. and Wagner,E.J. (2020) Integrator recruits protein phosphatase 2A to prevent pause release and facilitate transcription termination. *Mol. Cell.*, **80**, 345–358.
- Zheng,H., Qi,Y., Hu,S., Cao,X., Xu,C., Yin,Z., Chen,X., Li,Y., Liu,W., Li,J. *et al.* (2020) Identification of Integrator-PP2A complex (INTAC), an RNA polymerase II phosphatase. *Science*, **370**, eabb5872.
- Vervoort,S.J., Welsh,S.A., Devlin,J.R., Barbieri,E., Knight,D.A., Offley,S., Bjelosevic,S., Costacurta,M., Todorovski,I., Kearney,C.J. *et al.* (2021) The PP2A-Integrator-CDK9 axis fine-tunes transcription and can be targeted therapeutically in cancer. *Cell*, **184**, 3143–3162.
- Cossa,G., Parua,P.K., Eilers,M. and Fisher,R.P. (2021) Protein phosphatases in the RNAPII transcription cycle: erasers, sculptors, gatekeepers, and potential drug targets. *Genes Dev.*, **35**, 658–676.

12. Blazek,D., Kohoutek,J., Bartholomeeusen,K., Johansen,E., Hulinkova,P., Luo,Z., Cimermanec,P., Ule,J. and Peterlin,B.M. (2011) The cyclin K/Cdk12 complex maintains genomic stability via regulation of expression of DNA damage response genes. *Genes Dev.*, **25**, 2158–2172.
13. Krajewska,M., Dries,R., Grasseti,A.V., Dust,S., Gao,Y., Huang,H., Sharma,B., Day,D.S., Kwiatkowski,N., Pomaville,M. *et al.* (2019) CDK12 loss in cancer cells affects DNA damage response genes through premature cleavage and polyadenylation. *Nat. Commun.*, **10**, 1757.
14. Luyties,O. and Taatjes,D.J. (2022) The Mediator kinase module: an interface between cell signaling and transcription. *Trends Biochem. Sci.*, **47**, 314–327.
15. Gajduskova,P., Ruiz de Los Mozos,I., Rajecy,M., Hluchy,M., Ule,J. and Blazek,D. (2020) CDK11 is required for transcription of replication-dependent histone genes. *Nat. Struct. Mol. Biol.*, **27**, 500–510.
16. Hluchy,M., Gajduskova,P., Ruiz de Los Mozos,I., Rajecy,M., Kluge,M., Berger,B.T., Slaba,Z., Potesil,D., Weiss,E., Ule,J. *et al.* (2022) CDK11 regulates pre-mRNA splicing by phosphorylation of SF3B1. *Nature*, **609**, 829–834.
17. Bradner,J.E., Hnisz,D. and Young,R.A. (2017) Transcriptional addiction in cancer. *Cell*, **168**, 629–643.
18. Vervoort,S.J., Devlin,J.R., Kwiatkowski,N., Teng,M., Gray,N.S. and Johnstone,R.W. (2022) Targeting transcription cycles in cancer. *Nat. Rev. Cancer*, **22**, 5–24.
19. Zatzman,M., Fuligni,F., Ripsman,R., Suwal,T., Comitani,F., Edward,L.-M., Denroche,R., Jang,G.H., Notta,F., Gallinger,S. *et al.* (2022) Widespread hypertranscription in aggressive human cancers. *Sci. Adv.*, **8**, eabn0238.
20. Minzel,W., Venkatachalam,A., Fink,A., Hung,E., Brachya,G., Burstain,I., Shaham,M., Rivlin,A., Omer,I., Zinger,A. *et al.* (2018) Small molecules Co-targeting cki α and the transcriptional kinases CDK7/9 control AML in preclinical models. *Cell*, **175**, 171–185.
21. Quereda,V., Bayle,S., Vena,F., Frydman,S.M., Monastyrskyi,A., Roush,W.R. and Duckett,D.R. (2019) Therapeutic targeting of CDK12/CDK13 in triple-negative breast cancer. *Cancer Cell*, **36**, 545–558.
22. Zhang,H., Pandey,S., Travers,M., Sun,H., Morton,G., Madzo,J., Chung,W., Khowsathit,J., Perez-Leal,O., Barrero,C.A. *et al.* (2018) Targeting CDK9 reactivates epigenetically silenced genes in cancer. *Cell*, **175**, 1244–1258.
23. Wang,Y., Zhang,T., Kwiatkowski,N., Abraham,B.J., Lee,T.I., Xie,S., Yuzugullu,H., Von,T., Li,H., Lin,Z. *et al.* (2015) CDK7-dependent transcriptional addiction in triple-negative breast cancer. *Cell*, **163**, 174–186.
24. Chipumuro,E., Marco,E., Christensen,C.L., Kwiatkowski,N., Zhang,T., Hatheway,C.M., Abraham,B.J., Sharma,B., Yeung,C., Altshuler,A. *et al.* (2014) CDK7 inhibition suppresses super-enhancer-linked oncogenic transcription in MYCN-driven cancer. *Cell*, **159**, 1126–1139.
25. Morales,F. and Giordano,A. (2016) Overview of CDK9 as a target in cancer research. *Cell Cycle*, **15**, 519–527.
26. Boshuizen,J. and Peeper,D.S. (2020) Rational cancer treatment combinations: an urgent clinical need. *Mol. Cell*, **78**, 1002–1018.
27. Carneiro,B.A. and El-Deiry,W.S. (2020) Targeting apoptosis in cancer therapy. *Nat. Rev. Clin. Oncol.*, **17**, 395–417.
28. Bai,L. and Wang,S. (2014) Targeting apoptosis pathways for new cancer therapeutics. *Ann. Rev. Med.*, **65**, 139–155.
29. Galbraith,M.D., Bender,H. and Espinosa,J.M. (2019) Therapeutic targeting of transcriptional cyclin-dependent kinases. *Transcription*, **10**, 118–136.
30. Li,X., Huang,C.-H., Sánchez-Rivera,F.J., Kennedy,M.C., Tschaharganeh,D.F., Morris,J.P., Montinaro,A., O'Rourke,K.P., Banito,A., Wilkinson,J.E. *et al.* (2022) A preclinical platform for assessing antitumor effects and systemic toxicities of cancer drug targets. *Proc. Natl. Acad. Sci. U.S.A.*, **119**, e2110557119.
31. Olson,C.M., Jiang,B., Erb,M.A., Liang,Y., Doctor,Z.M., Zhang,Z., Zhang,T., Kwiatkowski,N., Boukhali,M., Green,J.L. *et al.* (2018) Pharmacological perturbation of CDK9 using selective CDK9 inhibition or degradation. *Nat. Chem. Biol.*, **14**, 163–170.
32. Vassilev,L.T., Vu,B.T., Graves,B., Carvajal,D., Podlaski,F., Filipovic,Z., Kong,N., Kammholt,U., Lukacs,C., Klein,C. *et al.* (2004) In vivo activation of the p53 pathway by small-molecule antagonists of MDM2. *Science*, **303**, 844–848.
33. Konopleva,M., Martinelli,G., Dayer,N., Papayannidis,C., Wei,A., Higgins,B., Ott,M., Mascarenhas,J. and Andreeff,M. (2020) MDM2 inhibition: an important step forward in cancer therapy. *Leukemia*, **34**, 2858–2874.
34. Pemovska,T., Kontro,M., Yadav,B., Edgren,H., Eldfors,S., Szwajda,A., Almusa,H., Bepalov,M.M., Ellonen,P., Elonen,E. *et al.* (2013) Individualized systems medicine strategy to tailor treatments for patients with chemorefractory acute myeloid leukemia. *Cancer Discov.*, **3**, 1416–1429.
35. Potdar,S., Ianevski,A., Mpindi,J.P., Bychkov,D., Fiere,C., Ianevski,P., Yadav,B., Wennerberg,K., Aittokallio,T., Kallioniemi,O. *et al.* (2020) Breeze: an integrated quality control and data analysis application for high-throughput drug screening. *Bioinformatics*, **36**, 3602–3604.
36. Yadav,B., Pemovska,T., Szwajda,A., Kuleskiy,E., Kontro,M., Karjalainen,R., Majumder,M.M., Malani,D., Murumägi,A., Knowles,J. *et al.* (2014) Quantitative scoring of differential drug sensitivity for individually optimized anticancer therapies. *Sci. Rep.*, **4**, 5193.
37. Ianevski,A., Giri,A.K. and Aittokallio,T. (2022) SynergyFinder 3.0: an interactive analysis and consensus interpretation of multi-drug synergies across multiple samples. *Nucleic Acids Res.*, **50**, W739–W743.
38. Bonfert,T., Kirner,E., Csaba,G., Zimmer,R. and Friedel,C.C. (2015) ContextMap 2: fast and accurate context-based RNA-seq mapping. *BMC Bioinform.*, **16**, 122.
39. Li,H. and Durbin,R. (2009) Fast and accurate short read alignment with Burrows-Wheeler transform. *Bioinformatics*, **25**, 1754–1760.
40. Liao,Y., Smyth,G.K. and Shi,W. (2014) featureCounts: an efficient general purpose program for assigning sequence reads to genomic features. *Bioinformatics*, **30**, 923–930.
41. Frankish,A., Diekhans,M., Jungreis,I., Lagarde,J., Loveland,J.E., Mudge,J.M., Sisu,C., Wright,J.C., Armstrong,J., Barnes,I. *et al.* (2021) GENCODE 2021. *Nucleic Acids Res.*, **49**, D916–D923.
42. Robinson,M.D., McCarthy,D.J. and Smyth,G.K. (2010) edgeR: a bioconductor package for differential expression analysis of digital gene expression data. *Bioinformatics*, **26**, 139–140.
43. Benjamini,Y. and Hochberg,Y. (1995) Controlling the false discovery rate: a practical and powerful approach to multiple testing. *J. R. Stat. Soc. Series B (Method.)*, **57**, 289–300.
44. Kluge,M. and Friedel,C.C. (2018) Watchdog - a workflow management system for the distributed analysis of large-scale experimental data. *BMC Bioinform.*, **19**, 97.
45. Murtagh,F. and Legendre,P. (2014) Ward's hierarchical agglomerative clustering method: which algorithms implement Ward's criterion? *J. Classif.*, **31**, 274–295.
46. Subramanian,A., Tamayo,P., Mootha,Vamsi,K., Mukherjee,S., Ebert Benjamin,L., Gillette Michael,A., Paulovich,A., Pomeroy Scott,L., Golub Todd,R., Lander Eric,S. *et al.* (2005) Gene set enrichment analysis: a knowledge-based approach for interpreting genome-wide expression profiles. *Proc. Natl. Acad. Sci.*, **102**, 15545–15550.
47. Ekumi,K.M., Paculova,H., Lenasi,T., Pospichalova,V., Bosken,C.A., Rybarikova,J., Bryja,V., Geyer,M., Blazek,D. and Barboric,M. (2015) Ovarian carcinoma CDK12 mutations misregulate expression of DNA repair genes via deficient formation and function of the Cdk12/CycK complex. *Nucleic Acids Res.*, **43**, 2575–2589.
48. Yadav,B., Pemovska,T., Szwajda,A., Kuleskiy,E., Kontro,M., Karjalainen,R., Majumder,M.M., Malani,D., Murumägi,A., Knowles,J. *et al.* (2014) Quantitative scoring of differential drug sensitivity for individually optimized anticancer therapies. *Sci. Rep.*, **4**, 5193–5193.
49. Longley,D.B., Harkin,D.P. and Johnston,P.G. (2003) 5-Fluorouracil: mechanisms of action and clinical strategies. *Nat. Rev. Cancer*, **3**, 330–338.
50. Tovar,C., Rosinski,J., Filipovic,Z., Higgins,B., Kolinsky,K., Hilton,H., Zhao,X., Vu,B.T., Qing,W., Packman,K. *et al.* (2006) Small-molecule MDM2 antagonists reveal aberrant p53 signaling in cancer: implications for therapy. *Proc. Natl. Acad. Sci. U.S.A.*, **103**, 1888–1893.
51. Bunz,F., Hwang,P.M., Torrance,C., Waldman,T., Zhang,Y., Dillehay,L., Williams,J., Lengauer,C., Kinzler,K.W. and

- Vogelstein, B. (1999) Disruption of p53 in human cancer cells alters the responses to therapeutic agents. *J. Clin. Invest.*, **104**, 263–269.
52. Lu, H., Xue, Y., Yu, G.K., Arias, C., Lin, J., Fong, S., Faure, M., Weisburd, B., Ji, X., Mercier, A. *et al.* (2015) Compensatory induction of MYC expression by sustained CDK9 inhibition via a BRD4-dependent mechanism. *Elife*, **4**, e06535.
 53. Kalan, S., Amat, R., Schachter, M.M., Kwiatkowski, N., Abraham, B.J., Liang, Y., Zhang, T., Olson, C.M., Larochelle, S., Young, R.A. *et al.* (2017) Activation of the p53 transcriptional program sensitizes cancer cells to Cdk7 inhibitors. *Cell Rep.*, **21**, 467–481.
 54. Mayer, A., di Iulio, J., Maleri, S., Eser, U., Vierstra, J., Reynolds, A., Sandstrom, R., Stamatoyannopoulos, J.A. and Churchman, L.S. (2015) Native elongating transcript sequencing reveals human transcriptional activity at nucleotide resolution. *Cell*, **161**, 541–554.
 55. Chao, S.H. and Price, D.H. (2001) Flavopiridol inactivates P-tef and blocks most RNA polymerase II transcription in vivo. *J. Biol. Chem.*, **276**, 31793–31799.
 56. Olson, C.M., Liang, Y., Leggett, A., Park, W.D., Li, L., Mills, C.E., Elsarraz, S.Z., Ficarro, S.B., Zhang, T., Duster, R. *et al.* (2019) Development of a selective CDK7 covalent inhibitor reveals predominant cell-cycle phenotype. *Cell. Chem. Biol.*, **26**, 792–803.
 57. Porter, D.C., Farmaki, E., Altiglia, S., Schools, G.P., West, D.K., Chen, M., Chang, B.D., Puzyrev, A.T., Lim, C.U., Rokow-Kittell, R. *et al.* (2012) Cyclin-dependent kinase 8 mediates chemotherapy-induced tumor-promoting paracrine activities. *Proc. Natl. Acad. Sci. U.S.A.*, **109**, 13799–13804.
 58. Lin, A., Giuliano, C.J., Palladino, A., John, K.M., Abramowicz, C., Yuan, M.L., Sausville, E.L., Lukow, D.A., Liu, L., Chait, A.R. *et al.* (2019) Off-target toxicity is a common mechanism of action of cancer drugs undergoing clinical trials. *Sci. Transl. Med.*, **11**, eaaw8412.
 59. Zhang, T., Kwiatkowski, N., Olson, C.M., Dixon-Clarke, S.E., Abraham, B.J., Greifengberg, A.K., Ficarro, S.B., Elkins, J.M., Liang, Y., Hannett, N.M. *et al.* (2016) Covalent targeting of remote cysteine residues to develop CDK12 and CDK13 inhibitors. *Nat. Chem. Biol.*, **12**, 876–884.
 60. Sur, S., Pagliarini, R., Bunz, F., Rago, C., Diaz, L.A. Jr., Kinzler, K.W., Vogelstein, B. and Papadopoulos, N. (2009) A panel of isogenic human cancer cells suggests a therapeutic approach for cancers with inactivated p53. *Proc. Natl. Acad. Sci. U.S.A.*, **106**, 3964–3969.
 61. Kastnerhuber, E.R. and Lowe, S.W. (2017) Putting p53 in context. *Cell*, **170**, 1062–1078.
 62. Dixon, A.S., Schwinn, M.K., Hall, M.P., Zimmerman, K., Otto, P., Lubben, T.H., Butler, B.L., Binkowski, B.F., Machleidt, T., Kirkland, T.A. *et al.* (2016) NanoLuc complementation reporter optimized for accurate measurement of protein interactions in cells. *ACS Chem. Biol.*, **11**, 400–408.
 63. Liberzon, A., Birger, C., Thorvaldsdóttir, H., Ghandi, M., Mesirov, J.P. and Tamayo, P. (2015) The Molecular Signatures Database (MSigDB) hallmark gene set collection. *Cell Syst.*, **1**, 417–425.
 64. Andrysik, Z., Galbraith, M.D., Guarnieri, A.L., Zaccara, S., Sullivan, K.D., Pandey, A., MacBeth, M., Inga, A. and Espinosa, J.M. (2017) Identification of a core TP53 transcriptional program with highly distributed tumor suppressive activity. *Genome Res.*, **27**, 1645–1657.
 65. Singh, R., Letai, A. and Sarosiek, K. (2019) Regulation of apoptosis in health and disease: the balancing act of BCL-2 family proteins. *Nat. Rev. Mol. Cell. Biol.*, **20**, 175–193.
 66. Tait, S.W. and Green, D.R. (2013) Mitochondrial regulation of cell death. *Cold Spring Harb. Perspect. Biol.*, **5**, a008706.
 67. Kale, J., Osterlund, E.J. and Andrews, D.W. (2018) BCL-2 family proteins: changing partners in the dance towards death. *Cell Death Differ.*, **25**, 65–80.
 68. Dorstyn, L., Akey, C.W. and Kumar, S. (2018) New insights into apoptosome structure and function. *Cell Death Differ.*, **25**, 1194–1208.
 69. Albert, T.K., Antrecht, C., Kremmer, E. and Meisterernst, M. (2016) The establishment of a hyperactive structure allows the tumour suppressor protein p53 to function through P-tef during limited CDK9 kinase inhibition. *PLoS One*, **11**, e0146648.
 70. Titov, D.V., Gilman, B., He, Q.L., Bhat, S., Low, W.K., Dang, Y., Smeaton, M., Demain, A.L., Miller, P.S., Kugel, J.F. *et al.* (2011) XBP, a subunit of TFIIF, is a target of the natural product triptolide. *Nat. Chem. Biol.*, **7**, 182–188.
 71. Fruman, D.A., Chiu, H., Hopkins, B.D., Bagrodia, S., Cantley, L.C. and Abraham, R.T. (2017) The PI3K pathway in Human disease. *Cell*, **170**, 605–635.
 72. Lawrence, M.S., Stojanov, P., Mermel, C.H., Robinson, J.T., Garraway, L.A., Golub, T.R., Meyerson, M., Gabriel, S.B., Lander, E.S. and Getz, G. (2014) Discovery and saturation analysis of cancer genes across 21 tumour types. *Nature*, **505**, 495–501.
 73. Mandelker, D., Gabelli, S.B., Schmidt-Kittler, O., Zhu, J., Cheong, I., Huang, C.H., Kinzler, K.W., Vogelstein, B. and Amzel, L.M. (2009) A frequent kinase domain mutation that changes the interaction between PI3Kalpha and the membrane. *Proc. Natl. Acad. Sci. U.S.A.*, **106**, 16996–17001.
 74. Datta, S.R., Brunet, A. and Greenberg, M.E. (1999) Cellular survival: a play in three Acts. *Genes Dev.*, **13**, 2905–2927.
 75. Folkes, A.J., Ahmadi, K., Alderton, W.K., Alix, S., Baker, S.J., Box, G., Chuckowree, I.S., Clarke, P.A., Depledge, P., Eccles, S.A. *et al.* (2008) The identification of 2-(1H-indazol-4-yl)-6-(4-methanesulfonyl-piperazin-1-ylmethyl)-4-morpholin-4-yl-thieno[3,2-d]pyrimidine (GDC-0941) as a potent, selective, orally bioavailable inhibitor of class I PI3 kinase for the treatment of cancer. *J. Med. Chem.*, **51**, 5522–5532.
 76. Sullivan, K.D., Padilla-Just, N., Henry, R.E., Porter, C.C., Kim, J., Tentler, J.J., Eckhardt, S.G., Tan, A.C., DeGregori, J. and Espinosa, J.M. (2012) ATM and MET kinases are synthetic lethal with nongenotoxic activation of p53. *Nat. Chem. Biol.*, **8**, 646–654.
 77. Zanoni, M., Piccinini, F., Arienti, C., Zamagni, A., Santi, S., Polico, R., Bevilacqua, A. and Tesei, A. (2016) 3D tumor spheroid models for in vitro therapeutic screening: a systematic approach to enhance the biological relevance of data obtained. *Sci Rep.*, **6**, 19103.
 78. Leonard, D., Huang, W., Izadmehr, S., O'Connor, C.M., Wiredja, D.D., Wang, Z., Zaware, N., Chen, Y., Schlatter, D.M., Kislar, J. *et al.* (2020) Selective PP2A enhancement through biased heterotrimer stabilization. *Cell*, **181**, 688–701.e616.
 79. Moreno, N., Holsten, T., Mertins, J., Zhong, C., Yuan, L., Guo, J., Meng, D., Chen, M. and Yao, L. (2020) CDK9 inhibitor CDKI-73 is synergistic lethal with PARP inhibitor olaparib in BRCA1 wide-type ovarian cancer. *Am. J. Cancer Res.*, **10**, 1140–1155.
 80. Poon, E., Liang, T., Jamin, Y., Walz, S., Kwok, C., Hakkert, A., Barker, K., Urban, Z., Thway, K., Zeid, R. *et al.* (2020) Orally bioavailable CDK9/2 inhibitor shows mechanism-based therapeutic potential in MYCN-driven neuroblastoma. *J. Clin. Invest.*, **130**, 5875–5892.
 81. Vainonen, J., Momeny, M. and Westermarck, J. (2021) Druggable cancer phosphatases. *Sc. Trans. Med.*, **13**, eabe2967.
 82. Beckerman, R. and Prives, C. (2010) Transcriptional regulation by p53. *Cold Spring Harb. Perspect. Biol.*, **2**, a000935.
 83. Wang, S. and El-Deiry, W.S. (2004) Inducible silencing of KILLER/DR5 in vivo promotes bioluminescent colon tumor xenograft growth and confers resistance to chemotherapeutic agent 5-fluorouracil. *Cancer Res.*, **64**, 6666–6672.
 84. Henry, R.E., Andrysik, Z., Paris, R., Galbraith, M.D. and Espinosa, J.M. (2012) A DR4:BIID axis drives the p53 apoptotic response by promoting oligomerization of poised BAX. *EMBO J.*, **31**, 1266–1278.
 85. Li, Y., Yang, J., Aguilar, A., McEachern, D., Przybranowski, S., Liu, L., Yang, C.Y., Wang, M., Han, X. and Wang, S. (2019) Discovery of MD-224 as a first-in-class, highly potent, and efficacious proteolysis targeting chimera Murine double minute 2 degrader capable of achieving complete and durable tumor regression. *J. Med. Chem.*, **62**, 448–466.
 86. Fulda, S. and Vucic, D. (2012) Targeting IAP proteins for therapeutic intervention in cancer. *Nat. Rev. Drug Discov.*, **11**, 109–124.